

1 **Hierarchical Domain Structure Reveals the Divergence of**

2 **Activity among TADs and Boundaries**

3
4 Lin An¹, Tao Yang¹, Jiahao Yang², Johannes Nuebler³, Guanjue Xiang¹, Ross C. Hardison⁴, Qunhua
5 Li^{5*}, Yu Zhang^{5*}

6
7 ¹Bioinformatics and Genomics program, Pennsylvania State University, University Park,
8 PA, ²Tsinghua University, Beijing, China, ³ Institute for Medical Engineering and Science,
9 Massachusetts Institute of Technology, Cambridge, MA, ⁴Department of Biochemistry and Molecular
10 Biology, Pennsylvania State University, University Park, PA, ⁵ Department of Statistics, Pennsylvania
11 State University, University Park, PA

12 *To whom correspondence should be addressed.

13
14 Email addresses:
15 LA: lua137@psu.edu; TY: txy146@psu.edu; JY: yangjh14@mails.tsinghua.edu.cn; JN:
16 jnuebler@mit.edu; RH: rch8@psu.edu; QL: qunhua.li@psu.edu; YZ: yzz2@psu.edu.

17
18 **Abstract**
19 The spatial organization of chromatin in the nucleus has been implicated in many aspects of
20 regulated gene expression. Maps of high frequency interactions between different segments of
21 chromatin have revealed Topologically Associating Domains (TADs), within which most of the
22 regulatory interactions are thought to occur. Recent studies have shown that TADs are not
23 homogeneous structural units, but rather they appear to be organized into a hierarchy. However,
24 precise identification of hierarchical TAD structures remains a challenge. We present OnTAD,
25 an Optimized Nested TAD caller from Hi-C data, to identify hierarchical TADs. Compared to
26 existing methods, OnTAD has significantly improved accuracy and running speed. Results from
27 OnTAD reveal new biological insights on the role of different TAD levels, boundary usage in
28 gene regulation, the loop extrusion model, and compartmental domains. The software and
29 documentation for OnTAD are available at: <https://github.com/anlin00007/OnTAD>

30
31 **Background**
32 Previous studies have shown that the human genome is spatially organized at different levels in
33 the nucleus, with each level of organization playing a role in gene regulation [1]. Starting with
34 the original Chromatin Conformation Capture (3C) assay [2] for measuring chromatin interaction

35 frequencies, many higher throughput, sequencing-based methods such as 4C, 5C, ChIA-PET,
36 Hi-C, and Hi-ChIP have been developed to measure 3D interaction frequencies at different
37 resolutions [3–8]. These maps of interaction frequencies between segments of chromatin are
38 interpreted in terms of chromatin structures. Among the methods, Hi-C [9] obtains measurement
39 of chromatin interaction frequencies across the entire genome. Within some local regions in a
40 genome, interactions are significantly higher than they are to adjacent regions; these highly
41 interacting regions are termed ‘Topologically Associating Domains’ (TADs) [10,11]. The proteins
42 CTCF and cohesin are frequently enriched at TAD boundaries, and they have been implicated
43 in the formation of an isolated local environment [11]. Furthermore, the positions of many TADs
44 are similar across different cell-types and even conserved between species [11,12]. As a result,
45 TADs have been widely interpreted as a basic architectural unit within which many gene
46 regulatory interactions occur. To date, several computational methods have been developed to
47 locate TADs in the genome. For example, Dixon et al. [11] developed a ‘Directionality Index’
48 based on the shift of interaction direction from upstream to downstream to estimate boundaries
49 of TADs. Other methods, such as TOPDOM [13] and Insulation Score [14], convert the TAD
50 boundary finding problem to a local minimum identification problem by calculating average
51 interaction frequency of surrounding regions at each locus.

52 While many earlier TAD calling methods treat TADs as a single structure, recent high-
53 resolution studies have shown that TADs contain internal substructures, with sub-TADs nested
54 within larger TADs [15–19]. Several recently developed TAD calling methods aimed to identify
55 nested TAD structures. For example, TADtree [15] identifies TADs based on a relationship
56 between the enrichment of contact frequency and TAD size, and assembles TADs into a TAD
57 tree that best fit the contact matrix. rGMAP [16] assumes that the interaction frequency in sub-
58 TADs is different from those in larger TADs, and applies a Gaussian Mixture model to identify
59 both types of TADs. Arrowhead [17] identifies corners of TADs at multiple sizes, allowing TADs
60 and subTADs to be detected simultaneously. 3D-Net [18] utilizes a maximization of network
61 modularity to identify TADs at different levels. And finally, IC-Finder [19] uses a hierarchical
62 clustering method to identify the TAD hierarchy.

63 Although the aforementioned methods provide useful tools for identifying TADs and their
64 internal substructure, we still lack comprehensive understanding of the functions of the
65 hierarchical structures within TADs. Recent work on low-resolution Hi-C data [20] has shown
66 that, at the large scale (> 1Mb), TADs can form a hierarchy of domains-within-domains
67 (“metaTAD”) through TAD-TAD interactions, and the successive levels of metaTAD organization
68 correlate with key epigenomic and expression features. This raises the natural question: do the

69 hierarchical levels within TADs also correlate with distinctive functional roles in chromosome
70 organization and gene regulation? However, most existing TAD callers focus on identifying the
71 locations of TADs and subTADs, rather than the hierarchical organization within TADs, making
72 them less suitable for investigating the biological functions of TAD hierarchy. Furthermore, many
73 existing callers are computationally inefficient for high-resolution Hi-C data and often lack a
74 principled approach to choosing algorithmic parameters [16]. These issues limit the utility of
75 existing TAD callers for investigating finer TADs structures using high-resolution data.

76 We present OnTAD, an Optimized Nested TAD caller that efficiently and robustly
77 uncovers hierarchical TAD structures from Hi-C data. Our approach first identifies candidate
78 TAD boundaries by scanning through the genome with a sliding window at a series of different
79 window sizes, using an approach inspired by TOPDOM [13]. Then, the candidate boundaries
80 are assembled into the optimized hierarchical TADs structures using a recursive dynamic
81 programming algorithm based on a scoring function. Our systematic evaluation shows that
82 OnTAD substantially outperforms existing TAD callers for both TAD boundary identification and
83 hierarchical TAD assembly. Using OnTAD, we uncovered novel insights on the potential
84 biological functions of TAD structures. In particular, we observed that active epigenetic states
85 are substantially more enriched in inner TADs than in outer TADs. OnTAD results revealed two
86 categories of TADs, those with or without hierarchical structures, that appear functionally distinct.
87 Compared to nonhierarchical TADs, the boundaries of TADs with hierarchical structures show a
88 higher CTCF enrichment, more active epigenetic states, and a higher level of gene expression.
89 In addition, we observed an apparent asymmetry in TAD boundary sharing, supporting the
90 asymmetric loop extrusion model for the formation of TADs [21]. Together, these results
91 demonstrate that OnTAD is a powerful tool for inferring different levels of chromatin organization
92 across a genome in high-resolution Hi-C data, which should facilitate improved investigations
93 into the roles of chromatin organization in gene regulation.

94

95 **Results**

96 **The OnTAD algorithm**

97 OnTAD takes a Hi-C contact matrix as the input and calls TADs in two steps. In the first step,
98 the method finds candidate TAD boundaries using an adaptive local minimum search algorithm
99 inspired by TOPDOM [13]. Specifically, it scans along the diagonal of a Hi-C matrix using a W
100 by W diamond-shaped window (Figure 1a), calculating the average contact frequency within
101 each window. The locations at which the average contact frequency reaches a significant local
102 minimum (1.96 standard deviations less than local maximum) are identified as candidate TAD

103 boundaries (see Methods). Because the sizes of TADs are unknown, OnTAD repeats the above
104 steps using a series of window-sizes, $W= 1,2,\dots,K$, to uncover all possible boundaries for TADs
105 in different sizes. Here, K depends on the resolution of the Hi-C matrix and the maximum TAD
106 size that the user aims to call. For instance, for a 10kb resolution Hi-C matrix and a maximum
107 TAD size of 2Mb, $K=2000/10=200$. The union of the candidate boundaries of all window sizes is
108 used to assemble TADs in the next step (Figure 1b).

109

110 In the second step, OnTAD assembles TADs by selectively connecting pairs of candidate
111 boundaries using a dynamic programming algorithm (see Methods). To form a TAD between a
112 pair of boundaries, OnTAD requires the mean contact frequency within the potential TAD area
113 between the boundaries to exceed that of the surrounding area outside of the TAD by a user-
114 defined margin (λ); otherwise, no TAD is formed between the boundaries. The dynamic
115 programming algorithm is formulated to recursively identify the optimal partition of the genome
116 for yielding the largest rightmost subTADs within each identified TAD according to a score
117 function (Supplementary Figure 1) that de-convolutes the contact frequency signals across the
118 TAD hierarchy (Supplementary Figure 2). At the end of the recursive procedure, the optimized
119 solution that maximizes the score function is obtained (defined in Methods), producing a
120 hierarchical TAD organization that best fits the observed Hi-C contact matrix. The locations of
121 the identified TADs are provided to the users as a plain text file and a bedgraph file ready for
122 visualization on genome browsers.

123

124 **Comparison with existing TAD calling methods**

125 We compared OnTAD with four representative TAD calling methods (DomainCaller, rGMAP,
126 Arrowhead and TADtree) using the Hi-C data in GM12878 from Rao et al.[17]. Each method
127 was run using the settings recommended in its manual (see Supplementary file 1 for the version
128 and parameters for each method). All the evaluations were performed using 10kb resolution for
129 the normalized genome-wide Hi-C data, unless specified otherwise. We also tested OnTAD on
130 raw data, and the results obtained were similar to those observed for normalized data
131 (Supplementary Figure 9).

132

133 *Accuracy of TAD boundary detection*

134 We first evaluated the accuracy of TAD boundary detection using enrichment of architectural
135 proteins at boundaries as a reference for accuracy. CTCF is an architectural protein implicated
136 in formation of TAD structures [10]. Thus, we expect a high concentration of CTCF signal (from

137 ChIP-seq data) at accurately called TAD boundaries. We computed the average CTCF ChIP-
138 seq signal in the boundaries identified by each TAD calling method as well as their
139 neighborhood regions. As shown in Figure 2a (left panel), all methods showed enrichment of
140 CTCF signal in the identified TAD boundaries over that in the surrounding regions (fold change >
141 1.63). Among them, OnTAD had the highest CTCF enrichment (mean signal 1.22X greater than
142 that of the second highest method, T-test p-value = 1.91e-28). A similar result was obtained for
143 the enrichment of the RAD21 and SMC3 subunits of the cohesin complex, which are also key
144 components in the formation of TADs [21]. The boundaries identified by OnTAD showed a
145 higher enrichment than those identified by other methods (mean signal 1.14X and 1.04X greater
146 than that of the second highest method, T-test p-value = 9.34e-16 and 1.91e-12, respectively)
147 (Figure 2a middle and right panel). The stronger enrichment of CTCF and cohesin signals
148 suggests that OnTAD produces more accurate calls of TAD boundaries than the other methods.
149

150 *Accuracy of TAD assembly*

151 We next evaluated the accuracy of TAD calling. If TADs are accurately called, one would expect
152 that a high proportion of the variation in the contact frequencies in the Hi-C matrix is explained
153 by TAD calls. We developed a metric called TAD-adjR², which is a modified version of the
154 adjusted R² (see Methods), to measure the proportion of Hi-C signal variation explained by TAD
155 calls. Because contact frequencies decay over the genomic distance between a pair of
156 interacting loci, we stratified the contacts by their genomic distance and calculated TAD-adjR²
157 within each stratum. As shown in Figure 2b, OnTAD has a higher TAD-adjR² than that of the
158 other methods across almost the entire span of genomic distances examined (0-1.5Mb)
159 (Average TAD-adjR²: OnTAD: 0.33, Arrowhead: 0.26, DomainCaller: 0.26, rGMAP: 0.23 and
160 TADtree: 0.06). This high level of explained Hi-C variance indicates that OnTAD produces a
161 better classification between TADs and non-TAD regions compared to other methods.
162

163 *Reproducibility of TAD calls and boundaries*

164 Another important criterion for TAD calling is the reproducibility of the identified TADs and their
165 boundaries. To measure the reproducibility of TAD boundaries, we calculated the agreement of
166 boundaries (Figure 2c-e) between two TAD calling results using the Jaccard index. To measure
167 the reproducibility of TADs, we treated each region covered by a TAD as a cluster of bins in the
168 genome, and then measured the agreement of cluster assignments between two TAD calling
169 results using the adjusted rand index (Supplementary Figure 3a-c). We evaluated the
170 reproducibility in three scenarios: 1) between biological replicates (GM12878, 10Kb) (Figure 2c,

171 Supplementary Figure 3a); 2) across different resolutions (5Kb, 10Kb, 25Kb) (Figure 2d,
172 Supplementary Figure 3b); and 3) at different sequencing depths (original sequencing depth
173 versus 1/4, 1/8, 1/16 and 1/32 of the total number of reads) (Figure 2e, Supplementary Figure
174 3c). As shown in Figure 2c-e and Supplementary Figure 3b, both the boundaries and the TADs
175 identified by OnTAD were fairly reproducible, consistently having either the highest or the
176 second highest Jaccard index or Adjusted Rand index in all scenarios.

177

178 *Run time comparison*

179 We recorded the run time of different methods on the same high-performance computing cluster
180 (Xeon E5-2680CPU and 72Gb RAM). OnTAD ran notably faster than all the other methods
181 (Supplementary Table 1). For example, it took OnTAD 655 seconds to analyze 10Kb resolution
182 data for the whole genome, which was 3X faster than Arrowhead, 24X faster than DomainCaller,
183 28X faster than rGMAP, and 263X faster than TADtree.

184

185 **Level of TAD hierarchy is related to gene activity and epigenomic states**

186 We systematically studied the biological features of the TAD hierarchy, again using the Hi-C
187 data in GM12878 from Rao et al.[17]. Overall, 75.7% of the genome was covered by the TADs
188 identified by OnTAD; the rest of the genome was not assigned to any TADs, and we refer to
189 these TAD-free regions as gaps. Among all TADs identified by OnTAD, the majority (92.2%)
190 contained or belonged to hierarchical structures, while a small fraction had no hierarchical
191 structure. We referred to the former as ‘hierarchical TADs’ or ‘nested TADs’, and the latter as
192 ‘singletons’ (Figure 3a). We hypothesized that chromatin organized into these two types of
193 TADs may be playing distinctive roles in regulation, and thus we examined their association with
194 various epigenetic marks.

195

196 *Boundaries of hierarchical TADs have a higher CTCF enrichment*

197 We first compared the CTCF enrichment (see Methods) at the boundaries of the two types of
198 TADs. Indeed, the boundaries of hierarchical TADs were substantially more enriched with CTCF
199 signal than singleton boundaries (Figure 3b) (mean CTCF signals are 3.51 and 2.25,
200 respectively, T-test p-value = 1.52e-18). This enrichment of CTCF signal arose from a higher
201 average number of CTCF peaks at the boundaries of hierarchical TADs. The mean number of
202 CTCF peaks per boundary of a hierarchical TAD was 0.451, whereas it was only 0.181 for
203 boundaries of singleton TADs (T-test p-value = 4.52e-30).

204

205 *Hierarchical TADs have a stronger association with active epigenetic states*
206 Chromatin interactions are strongly associated with local, active epigenetic profiles [12,17, 22].
207 We thus expected to observe a positive association between the enrichment of active epigenetic
208 states and the levels of TADs. Starting with the 36 epigenetic states defined by IDEAS
209 segmentation [23] on 6 ENCODE cell lines, we evaluated the association between active
210 epigenetic states and TAD hierarchies. We classified hierarchical TADs into five levels, with
211 level one being the outermost TADs, level two being the immediate subTADs nested under one
212 layer of level one TAD, and so forth until level five, which contains the subTADs nested under
213 four or more layers of TADs in the hierarchy. We observed that the proportion of active
214 epigenetic states increase along the levels of TADs (Figure 3c, d). In contrast, singletons are
215 notably less active compared with hierarchical TADs (especially when level >2). In fact,
216 singleton TADs showed enrichments similar to those for the gap regions. A similar pattern of
217 enrichment for active states in hierarchical TADs was also observed in other cell types (K562
218 and HUVEC) (Supplementary Figure 4). Taken together, our results showed that hierarchical
219 TADs are on average more active than singletons; and within hierarchical TADs, inner TADs
220 (e.g., subTADs) are more active than outer TADs.

221

222 *Hierarchical TADs have more active gene expression*

223 We further investigated how gene expression is associated with TAD hierarchies. Using the
224 RNA-seq data of GM12878 from the ENCODE consortium (www.encodeproject.org) [24], we
225 defined expressed genes as those with FPKM > 5. Then within TADs at each level, we
226 computed the density of expressed genes (the number of expressed genes per bin, i.e., 10Kb
227 region). If a gene was covered by more than one TAD, we associated it with the innermost
228 TADs. We found that, as the TAD level increases, the density of expressed genes also
229 increases, i.e., genes are more frequently activated within inner TADs than outer TADs (ANOVA
230 test p-value of < 2.2e-16) (Figure 3e). Similarly, we observed the same trend of positive
231 association between density of expressed genes and the TAD level (ANOVA test p-value <
232 2.2e-16) in the K562 cell line (Figure 3f).

233

234 **Shared TAD boundaries are asymmetric and more active than other boundaries**

235 It has been reported that TAD boundaries are interaction hotspots [25]. We also observed that,
236 for TADs at all levels, the number of expressed genes and the enrichment of active epigenetic
237 states are significantly higher at the TAD boundaries than at the internal regions of TADs (all T-

238 test p-values < 0.001) (Supplementary Figure 5a&b). Thus we undertook an additional analysis
239 of TAD boundaries.

240 We observed that the boundaries of hierarchical TADs were frequently shared by
241 multiple TADs. We hypothesized that the boundary usage may play an important role in
242 maintaining hierarchical structures and regulating gene activities. To investigate this hypothesis,
243 we classified boundaries into five categories, according to the maximum number of TADs that
244 use a boundary on one of the two sides of the boundary (Figure 4a). A boundary is classified as
245 level one if it is used by no more than one TAD on either side, level two if it is used by exactly
246 two TADs on one side and less or equal to two TADs on the other side, and so forth to level five
247 if it is used by five or more TADs on either side. For example, a boundary shared by two TADs
248 to its left and three TADs to its right was classified as level three. The number of boundaries
249 assigned to each category is shown in Supplementary Figure 7.

250

251 *Epigenetic and genomic profiles*

252 We examined the enrichment of active epigenetic states at different boundary levels. We
253 observed a significant positive correlation between the enrichment (fold change) of active
254 epigenetic states and the number of times each boundary is shared (e.g., Tss state: Pearson
255 coefficient = 0.89; TssCtcf state: Pearson coefficient = 0.92) (Figure 4b). We further studied the
256 relationship between gene expression level and boundary sharing. Again, we observed a
257 significant positive association between the number of times a boundary was shared and the
258 gene expression level (ANOVA test p-value = 1.97e-05). In particular, the gene expression level
259 at the boundaries that were shared by 5 or more TADs was substantially higher than that at
260 boundaries that were shared by fewer TADs (Figure 4c). At a higher level boundary, multiple
261 genomic loci (the boundary plus the other ends of the TADs) must be in proximity in three-
262 dimensional space. This situation is reminiscent of chromatin hubs, and thus, we call the
263 boundaries shared by 5 or more TADs “hub-boundaries”. We posited that hub-boundaries are
264 more active in gene regulation than boundaries that are shared by fewer TADs.

265

266 *The asymmetric loop extrusion model*

267 Interestingly, we also observed some asymmetry in boundary usage and TAD formation in
268 hierarchical TADs. Specifically, we have observed (1) a significant difference in boundary usage
269 between the left and the right boundaries of the same outer TAD (Z-test p-value < 2.2e-16) and
270 (2) a significant difference in the numbers of TADs formed by a boundary on its left and right
271 sides (Z-test p-value < 2.2e-16) (Supplementary Table 2).

272 We therefore asked if the observed asymmetry is related to the mechanism of loop formation. A
273 recent study in yeast suggested that loops are formed in an asymmetric process, where the loop
274 extrusion complex anchors on one side and DNA reels through from the other side [26]. We
275 here hypothesize that loop extruders are preferentially loaded at or near a specific TAD
276 boundary. Then the asymmetric loop extrusion would start from this site on one end, and it
277 could stop at different sites on the other end. Thus, the TADs formed by multiple stops of loop
278 extrusion in this process would all share the anchor site as the boundary on one side, but each
279 has a different boundary on the other side, leading to the observed asymmetric boundary usage
280 (Figure 4d). Another recent study in *Drosophila* Schneider 2 (S2) cells showed that promoters
281 prefer to interact with enhancers downstream of the transcriptional unit [27], leading to a
282 directional preference in TAD formation. Indeed, as shown in Figure 4b, the boundaries shared
283 by multiple TADs are highly enriched with promoters, thus the observed orientation asymmetry
284 in TAD formation around these boundaries could reflect this interaction preference in promoters.
285

286 While some proteins (e.g. Ycg1 HEAT-repeat and Brn1 kleisin subunits) have been found to be
287 related to the anchor sites in yeast [28], little is known about the proteins supporting the anchor
288 sites in human. We therefore performed a transcription factor (TF) enrichment analysis using
289 161 TF ChIP-seq data from the ENCODE consortium [29–31]. By comparing the fold
290 enrichment of each TF signal in hub-boundary (level 5) with the ones at low level (level 1), we
291 found a group of TFs that were highly enriched in hub-boundaries (Fold Change > 2 in either
292 GM12878 (n = 8) or K562 (n = 37)) (Figure 4e). These hub-boundary-enriched TFs were
293 strongly associated with chromosome organization function in Gene Ontology Analysis (FDR =
294 1.33e-06). They were also shown to be highly connected (p-value < 1.0e-16) in the protein-
295 protein interaction database, STRING (Supplementary Figure 7), suggesting that they may
296 potentially form a protein complex. Together, these results suggest that the enriched TFs may
297 play an important role in forming the anchor sites in the asymmetric extrusion process.
298

299 **Hierarchical TAD calling unveils distinct epigenetic features of inner TADs**

300 It has been reported that genomic loci within the same TADs tend to possess similar epigenetic
301 features [22], while loci in different adjacent TADs may show different epigenetic features [17].
302 However, it remains unclear if the divergence of epigenetic profiles also takes place at the
303 subTAD level. To explore the possible answer to this question, we performed OnTAD on Hi-C
304 data from the mouse G1E-ER4 cell [32]. We observed that the majority of TADs (87.1%) are in
305 active compartments. As shown in the OnTAD genome browser track in Figure 5, the region of

306 (chr19:11.3Mb – 12.2Mb) contains multiple nested TADs. Among them, two adjacent subTADs
307 (11.8Mb – 11.9Mb and 11.9Mb – 12.0Mb) that belong to the same outer TAD (chr19: 11.5Mb –
308 12.0Mb) exhibit distinct epigenetic features, with enriched repressive epigenetic signal
309 (H3K27me3) in the left subTAD and enriched active epigenetic signal (H3K27ac, H3K4me3 and
310 H3K36me3) in the right subTAD. This demonstrates that, although TADs were traditionally
311 considered to be a fundamental unit of chromatin organization, epigenetic features can be
312 distinctively different between subTADs. Our results show that the subTADs identified by
313 OnTAD better represent homogeneous units associated with epigenetic functions, capturing
314 distinct functional features within subTADs. By identifying these subTADs, OnTAD enables a
315 finer investigation of the hierarchy of chromatin organization and its functionally homogeneous
316 structures.

317

318 Interestingly, we observed that whereas the outer TAD (11.8Mb – 12.0Mb) had clear CTCF
319 signals at its boundaries, the shared boundary between the two subTADs (11.8Mb – 11.9Mb
320 and 11.9Mb – 12.0Mb) had no CTCF signals from the CTCF ChIP-seq data. This indicates that
321 the formation of these two subTADs is probably independent of CTCF. Furthermore, we
322 performed a high-resolution compartment analysis (See Methods). It showed that the two
323 subTADs fall in different compartments. These results can be interpreted within the framework
324 of recently proposed ‘compartmental domains’ [33,34], which are hypothesized to be formed by
325 A/B compartment without the involvement of CTCF. We will discuss this mechanism further in
326 the discussion.

327

328 **Discussion**

329 While hierarchical structures in TAD formation have been reported [15,16,18,19], the
330 involvement of these hierarchies in gene regulation mechanisms remains poorly understood.
331 This is partly due to the lack of a method that systematically identifies TAD hierarchies from Hi-
332 C data and investigates the association of TAD hierarchies with epigenetic features. Here we
333 introduce OnTAD, a new method to uncover the hierarchical TAD structures from Hi-C data.
334 Based on a dynamic programming procedure that recursively finds the best domain partition of
335 Hi-C contact matrix in a hierarchical manner, OnTAD identifies the hierarchy of TADs and their
336 boundaries. It produces a convenient output for visualizing the hierarchy in a genome browser,
337 greatly facilitating the investigation of the interplay between hierarchical TADs and other
338 epigenetic features in gene regulation. Our comprehensive evaluation shows that OnTAD
339 substantially outperforms the existing TAD calling methods in both accuracy and computational

340 efficiency. These results demonstrated the effectiveness of OnTAD for identifying TAD
341 hierarchies and investigating their biological functions.

342
343 Using the results from OnTAD, we investigated how hierarchies within TADs were associated
344 with features related to function. In particular, we observed that, on average, hierarchical TADs
345 were significantly more active than TADs without hierarchies (i.e. singletons). The active
346 epigenetic states and active genes were also significantly more enriched in the boundaries
347 shared by multiple TADs (e.g. hub-boundaries) than those used exclusively by a single TAD.
348 These observations echo those on the hierarchy of metaTADs, which also showed a positive
349 association between the enrichments in promotor activity and gene density and boundary usage
350 [20]. Interestingly, we also observed a significant asymmetry in boundary usage between the left
351 and right boundaries in the hierarchical TADs and an asymmetry in the orientation of TAD
352 formation around hub-boundaries, supporting the asymmetric loop extrusion model [26] and
353 preferential orientation of promoter interaction [27].

354
355 Our results pose several interesting questions about the mechanisms utilized to form these
356 structures. First, how are these hierarchical TADs structures formed? Are they produced by
357 hierarchical chromatin folding in single cells, or does the nesting reflect a collection of different
358 interaction patterns in individual cells that looks like a hierarchy when the data from a population
359 of cells is aggregated in bulk cell Hi-C data? Single-allele chromatin interactions do reveal
360 regulatory hubs [35], supporting the interpretation that these complex interactions occur in
361 individual cells. A recent single-cell analysis of high-throughput Oligopaint labeling and imaging
362 on Chr21 of A549 cell, showed that both TAD and sub-TAD structures exist in single cells [36].
363 Furthermore, nested TAD structures could be formed by multi-site interactions in a single cell
364 [36]. However, as acknowledged by the authors, it is still possible that some other domain
365 structures resulted from population averaging. In principle, OnTAD can also be applied to
366 single-cell Hi-C data to explore this question. However, the genome coverage in current single-
367 cell Hi-C data is still low and can only support the analysis at the resolution of ~100Kb, limiting
368 the detection of finer domain structures (typically ~50Kb for subTADs we identified). Future
369 studies with higher resolution single-cell Hi-C data will be valuable for addressing this question
370 at a genome-wide scale.

371
372 Second, what are the mechanisms to form the hierarchical structures? As observed in our
373 analyses (Figure 5), though the majority of the outer TAD boundaries were bound by CTCF,

374 some subTADs appear to be formed without CTCF binding at their boundaries. The formation
375 of the latter can be explained by the recently proposed ‘compartmental domains’ mechanism
376 [34], which forms domains by establishing A/B compartments without the involvement of CTCF
377 or loop extrusion. Because OnTAD does not rely on CTCF information for TAD identification, it
378 can capture all domain structures, regardless the formation mechanisms. The example in Figure
379 5 could be explained by joint processes of loop extrusion (for the outer TAD) and establishment
380 of ‘compartmental domains’ [34] for the inner TADs.

381

382 In summary, we have demonstrated that the hierarchies of TAD structures are
383 associated with gene regulation and have provided a powerful tool for exploring this association.
384 Though previous results based on low-resolution data suggest that the majority of TAD
385 structures are conservative across cell lines [11], recent analyses found that certain locally
386 frequent interaction regions within TADs are cell type specific [25]. It will be particularly
387 interesting to use OnTAD to systematically investigate how the finer domain structures within
388 TADs differ across cell types, for example, how the levels of hierarchy differ across cell types,
389 and how the changes in hierarchy are associated with differential gene regulation. The
390 biological insights generated by analyses of the finer domain structures should help improve our
391 understanding of the role of chromatin conformation in gene regulation.

392

393

394 **Methods**

395 **Notations and data preprocessing**

396 Let X denote a symmetric Hi-C matrix, where each entry (i,j) in the matrix is a value quantifying
397 the strength of the chromatin interaction of between bins i and j . The Hi-C matrix can be raw
398 contact matrix or the normalized matrix produced by the normalization procedures such as ICE
399 [37] and KR [17]. Let $X[a:b, c:d] = \{(i,j) : a \leq i \leq b, c \leq j \leq d\}$ denote a sub-matrix of X . A candidate
400 TAD between bins a and b corresponds to a diagonal block matrix $X_{[a,b]} = X[a:b, a:b]$, where the
401 mean of the entries in $X_{[a,b]}$ is expected to be higher than that in its neighboring matrices.
402 Because of the distance dependency in Hi-C data, i.e., the dependence of contact frequency on
403 the proximity of the interaction loci, we normalize the Hi-C matrix before TAD calling by
404 subtracting the mean counts at each distance.

405

406 **Identification of candidate TAD boundaries**

407 We identify candidate TAD boundaries using a procedure motivated from the TOPDOM method
408 [13]. This procedure scans the diagonal of the Hi-C matrix, using a sliding square submatrix
409 whose bottom corner locates on the diagonal (Figure 1a), and computes the mean Hi-C signals
410 covered by the submatrix at each location, which is the TOPDOM statistic in [13]. As shown in
411 [13], when the corner of the submatrix lands on a TAD boundary, the TOPDOM statistic reaches
412 a local minimum. Thus, the local minimums of the TOPDOM statistic can be used as candidate
413 boundaries. The original TOPDOM paper only computed the statistics at a fixed window size. To
414 identify all candidate TAD boundaries for TADs in different sizes, the TOPDOM statistics are
415 calculated at all window sizes (W), ranging from 1 to a maximum TAD size (d) specified by
416 users. Here, we set the minimum size =3 bins, because structures smaller than 3 bins are too
417 small to form a domain. We set the maximum size=200 for 10kb Hi-C data, because TADs are
418 known to be smaller than a few Mbs.

419 For each window size W , we first obtained a set of local minimums of the TOPDOM statistics,
420 which are defined as the smallest value in the neighborhood of $[i-Lsize, i+Lsize]$. To reduce
421 false positives due to noise, the local minimums that are not significantly smaller than the local
422 maximums in the same neighborhood are pruned. Here we required the local minimums to be at
423 least $1.96S$ smaller than the local maximums to be qualified as a candidate boundary, where S
424 is the standard deviation of the TOPDOM statistic in the entire matrix. The parameter 1.96 is
425 chosen based on the 95% confidence level of a normal distribution, which reasonably
426 approximates the distribution of TOPDOM scores.

427 Figure 1b shows examples of the local minimums on the genome at different window sizes.
428 Because different window sizes capture the information of TADs in different sizes, we took the
429 union of the pruned local minimums over all window sizes, and used the corresponding bins as
430 candidate TAD boundaries. We selected z according to the procedure described in the section
431 of Parameter Selection. For all the analyses in this work, we used $Lsize = 5$. It can be adjusted
432 by users.

433

434 **Recursive TAD calling algorithm**

435 We developed a TAD calling algorithm to assemble TADs from the candidate boundaries.
436 Several issues need to be considered in the design of the algorithm in order to produce
437 biologically meaningful TADs. First, because a region may be shared by multiple TADs, the
438 scores of these TADs can be strongly correlated. Second, in the TADs with nested structures,
439 the scores of the TADs and their nested sub-TADs are convoluted. Third, some boundaries may

440 be shared between TADs. Last, the algorithm needs to be computationally efficient to call TADs
441 in the genome scale.

442 To address these issues, we developed a recursive algorithm to identify the TADs that give the
443 optimal partition of the genome according to a scoring function $g(X)$ related to the strength of Hi-
444 C signals (see the next section). Our algorithm assumes that any given two TADs are either
445 disjoint (but can share one boundary) or nested (i.e. one TAD is completely within the other).
446 This assumption is required for the dynamic programming to find an optimal solution in
447 polynomial time. While this assumption sometimes may not be true, it greatly reduces the
448 complexity of the problem while still enabling us to 1) de-convolute nested TAD structures, 2)
449 impose shared boundaries, and 3) obtain an efficient algorithmic solution. Our evaluation
450 showed that the majority of the genome follows this assumption (see the subsection below).
451 Even when it is violated, i.e., the boundaries of the TADs cross each other, our method can still
452 produce a reasonable approximation (Supplementary Fig.1C).

453 Briefly, the algorithm works as follows. Given a matrix $X_{[a,b]}$, the algorithm starts at the root level
454 to first find the best bin i ($a \leq i < b$) to partition the matrix into two submatrices, $X_{[a,i]}$ and $X_{[i,b]}$, such
455 that $X_{[i,b]}$ is the largest right-most TAD in $X_{[a,b]}$. Since $X_{[a,i]}$ and $X_{[i,b]}$ are disjointed, the TADs
456 within each submatrix can be called separately in a recursive manner. At each recursive step,
457 the parent matrix is partitioned into two sub-matrices, and TADs are called within each sub-
458 matrix using the same recursive formula (Supplementary Fig.2A). The recursion stops when $i=a$,
459 i.e., the sub-matrix $X_{[a,i]}$ contains no TAD. After a recursive step is completed, it identifies the
460 best TADs in the current branch according to the scoring function, de-convolutes the TAD
461 signals in the parent matrix by removing signals of inner TADs, and evaluates if the parent
462 matrix itself is a TAD. This process is repeated until the recursion returns to the root level
463 (Supplementary Fig.2B). Note that, because every TAD is the largest right-most TAD of a parent
464 matrix in a recursive branch, this recursive procedure guarantees to traverse all TADs, even
465 though only the largest right-most TAD is called at each step.

466

467 *Evaluation of the violation of the hierarchical TAD assumption*

468 To investigate the frequency of the violation of the hierarchical TAD assumption, we ran OnTAD
469 on high resolution (10Kb) in-situ Hi-C data in GM12878. We segregated regions around the
470 corner of each TAD into four 5*5 quadrants and calculated the average contact frequency of
471 each quadrant (Supplementary figure 8). If this assumption holds, the interaction frequency is
472 expected to be high in the quadrant within TAD (quadrant 1) and relatively low in at least one of
473 the two quadrants (2 & 3) on the two sides outside of TAD corner. As shown in the

474 Supplementary figure 8, the mean frequency patterns of the four quadrants for most of the TAD
475 corners are consistent with our expectations. This suggests that this assumption holds for a
476 majority of the genome. The violation can be remedied by removing the signals from the called
477 TADs and then rerunning OnTADs on the de-clumped Hi-C data to identify additional TADs.
478

479 **The scoring function**

480 Our scoring function $g(X_{[a,b]})$ for matrix $X_{[a,b]}$ is defined as

$$481 \quad g(X_{[a,b]}) = \max_i \begin{cases} 0 & i = a \\ \max \left(0, g(X_{[a,i]}) + h(X_{[i,b]}) \right) & i = a + 1, \dots, b - 1 \end{cases} \quad (1)$$

482 where $h(X_{[i,b]}) = g(X_{[i,b]}) + \Delta(X_{[i,b]}|\text{sub TADs})$

483 Here, $g(X_{[a,b]})$ is the score of TADs within $X_{[a,b]}$, not including the score for $X_{[a,b]}$ itself being a
484 TAD. It is calculated by finding the best left boundary of the largest right-most TAD in $X_{[a,b]}$.
485 $h(X_{[i,b]})$ is the score of the largest right-most TAD in $X_{[a,b]}$. It is the sum of the score of TADs
486 within $X_{[i,b]}$ and the score of $X_{[i,b]}$ itself being a TAD, namely $\Delta(X_{[i,b]}|\text{sub TADs})$. For any
487 diagonal block matrix to be called a TAD, its mean signal is required to be greater than the
488 means of its neighboring regions on both sides. We therefore define
489

$$\begin{aligned} \Delta(X_{[i,b]}|\text{sub TADs}) \\ = m(X_{[i,b]}|\text{sub TADs}) \\ - \max(\overline{X[(i-(b-i+1)):((b-(b-i+1)), i:b], X[i:b, (i+(b-i+1)):((b+(b-i+1))])}) - \lambda \end{aligned}$$

490
491 where $m(X_{[i,b]}|\text{sub TADs})$ denotes the mean of $X_{[i,b]}$, excluding the TADs within $X_{[i,b]}$, returned by
492 the recursion; λ is a user-specified nonnegative penalty parameter ;
493 $X[(i-(b-i+1)):((b-(b-i+1)), i:b]$ and $X[i:b, (i+(b-i+1)):((b+(b-i+1)))]$ are two $(b-i+1)$ -by- $(b-i+1)$ off-
494 diagonal matrices in the adjacent flanking regions of $X_{[i,b]}$; and finally, and \overline{X} denotes the mean
495 of X . We note that $\Delta(X_{[i,b]}|\text{sub TADs})$ is calculated based on the TADs returned from $g(X_{[i,b]})$.
496 That is, we do not directly optimize $g(X_{[i,b]}) + \Delta(X_{[i,b]}|\text{sub TADs})$. The parameter λ serves as a
497 threshold for TAD calling. That is, a TAD will be called only when the mean contact frequency
498 within the potential TAD area between the boundaries exceeds that of the surrounding area
499 outside of the TAD by the margin of λ . The procedure for selecting λ is described in Parameter
500 Selection.

501 When the score of a candidate TAD is <0, it is likely not a real TAD. We therefore set a lower
502 bound on the score at 0 and do not output the “TAD” with a score 0.

503

504 **Parameter Selection**

505 We selected the value of λ based on the False Discovery Rate (FDR) of TADs identification.
506 The FDR is calculated as follows. First, the entries in the real Hi-C matrix are permuted within
507 each genomic distance. This results in a null Hi-C matrix that has the same marginal signal
508 distribution as the original Hi-C matrix but without biologically meaningful TAD structures. Next,
509 OnTAD is run on both the original and the permuted Hi-C matrix for a series of λ . The TADs
510 identified from the original Hi-C matrix are treated as ‘discoveries’ (R), which is a mixture of
511 false and true discoveries, and those from the permuted Hi-C matrix are treated as ‘false
512 discoveries’ (V), which is used to approximate the proportion of false discoveries in R. Recall
513 that OnTAD assigns each TAD a score according to the scoring function (1). Given a TAD size,
514 the magnitude of the score reflects the strength of evidence to call TAD. Because larger TADs
515 tend to have a lower mean contact frequency after removing their inner TADs, the score is
516 usually smaller for larger TADs. Therefore, we computed the FDR accounting for TAD size.
517 Specifically, for a given value of λ , the identified TADs are first stratified by their sizes and
518 scores. Let n be the total number of TADs identified on the original matrices, and R_i and V_i be
519 the numbers of TADs in the i th stratum from the original and the permuted matrices,
520 respectively. Then if a TAD (j) is in the i th stratum, the probability for the TAD to be a false
521 discovery (a.k.a. local false discovery rate [38] is

522
$$p_j = \min\left(\frac{V_i}{R_i}, 1\right)$$

523 The overall FDR for the TAD identification is computed as the average of the probability to be a
524 false discovery over all TADs identified on the original matrix, based on the relationship between
525 local fdr and FDR [38]:

$$FDR = \frac{\sum_{j=1}^n p_j}{n}$$

526 The above FDR calculation is repeated for each value of λ , and the λ corresponding to the FDR
527 cutoff of 0.05 is selected.

528 In our analysis, the stratum is formed by dividing the TAD calls into 25 equal shares according
529 to the ranking of TAD size (or TAD score, respectively) on the real matrix. This leads to
530 $25 \times 25 = 625$ strata in total. As shown in Supplementary table 3, the FDR is close to 0.05 at $\lambda =$
531 0.1 for GM12878 dataset (10kb). To test the robustness of the tuned parameter, we also
532 performed the same procedure on the mouse G1E-ER4 Hi-C data from Hsu et al. [32] at 10Kb

533 resolution. The FDR was also controlled at the 0.05 level when $\lambda = 0.1$ (Supplementary table 4).
534 Therefore, we used $\lambda = 0.1$ as the default value in our analyses. In the OnTAD software, we
535 allow users to specify the value of λ to offer more flexibility.
536 Another important tuning parameter is Lsize, which is the span of the interval (i.e. the interval
537 size = $2*Lsize + 1$) for searching local minimums of the TOPDOM statistics. This parameter
538 affects the selection of candidate boundaries. If Lsize is too large, some potential boundaries
539 will be missed. If Lsize is too small, the candidate boundary set may include many false
540 positives, increasing the computational burden for the assembly step and the quality of final
541 results. We chose Lsize in the similar way as for choosing λ on GM12878 data (10kb).
542 Specifically, we ran OnTAD for different values of Lsize (range=3-10), corresponding to the
543 interval size of 7-21 bins. We chose this range because it is sufficient to cover various TAD
544 sizes. As shown in Supplementary table 5, Lsize=5 (i.e. interval size=11) renders an FDR close
545 to 0.05. Therefore, we chose Lsize=5 for all analyses. To evaluate the robustness of this choice,
546 we evaluate the similarity of the identified TAD structures between Lsize=5 and Lsize=6-10, and
547 found that they are similar, with the median of the adjusted rand indices >0.75 (Supplementary
548 figure 10). It indicates the result is relatively insensitive to the value of Lsize when Lsize=5~10.
549

550 **Computation complexity of the TAD calling algorithm**

551 We performed an analysis on the computational complexity for our recursive algorithm. For an
552 $l \times l$ Hi-C matrix, if all bins are potential boundaries, then the recursion needs to visit $l(l+1)/2$
553 diagonal block sub-matrices. As there are l size 1 diagonal block matrices, the computation
554 complexity for computing the scores of all size 1 matrices is $O(l)$. Given the scores of size 1
555 matrices, we can calculate the scores of size 2 matrices. There are $(l-1)$ of them, each
556 enumerating through $(2-1)$ partitions. Hence the time complexity is $O((2-1)(l-1))$. Following the
557 same calculation, the scores of one sub-matrix of size k will be computed by enumerating $(k-1)$
558 partitions. As there are $(l-k+1)$ of them, the time complexity is $O((k-1)(l-k+1))$. Similar calculation
559 can be done for the mean of sub-matrices. As a result, the total complexity to obtain the scores
560 of all sub-matrices from size 1 to l is $O(l^3)$.

561 Empirically, the computational complexity is much lower than the above due to some further
562 reductions. First, because potential TAD boundaries are limited to the TOPDOM local minimums,
563 this substantially reduces the number of partitions from $O(l^3)$ to $O(m^3)$, where m is the number of
564 candidate boundaries. Second, because TADs usually are smaller than 2Mb, the maximum TAD
565 size to be called (d) typically is much smaller than l . This constraint effectively reduces the time
566 complexity of our algorithm from $O(m^3)$ to $O(md^2)$. Furthermore, because TADs usually are

567 formed between neighboring boundaries, we set a constraint in the recursive procedure to limit
568 the TADs to be formed only between candidate boundaries that are no more than five neighbors
569 apart.

570

571 **TAD-adjR² for assessing accuracy of TAD calling**

572 Because TADs are regions with frequent local interactions, a reasonable TAD caller is expected
573 to classify the regions with high contact frequencies as TADs and the regions with low contact
574 frequencies as non-TADs, i.e. gaps between TADs. At any given genomic distance, the
575 variation between Hi-C signals should be largely explained by the classification of TADs. How
576 well the variation can be explained by the classification of TADs can reflect the accuracy of TAD
577 calling. Based on this intuition, we developed a metric similar to the R-square in regression
578 models to evaluate the accuracy of TAD calling. Let Y_i denote the contact frequency of the i th
579 bin, n denote the number of bins at the same genomic distance as this bin, p denotes the
580 number of called TADs whose sizes are greater than or equal to the genomic distance. For bins
581 within TAD, \hat{Y}_i denotes the average contact frequency at given genomic distance within that
582 TAD, excluding regions covered by higher level TADs. For those bins not in any TADs, \hat{Y}_i is the
583 average of contact frequency in the gap region at that genomic distance. And \bar{Y} denote the
584 overall mean contact frequency across all the bins at a given genomic distance. For each
585 genomic distance, the TAD-adjR² is defined as

$$\hat{R}_{tad}^2 = 1 - \frac{\frac{1}{n-p-1} \sum_{i=1}^n (Y_i - \hat{Y}_i)^2}{\frac{1}{n-1} \sum_{i=1}^n (Y_i - \bar{Y})^2}$$

586 This quantity essentially measures the proportion of variance in Hi-C signal that is explained by
587 the classification of TADs, adjusting for the number of TADs and genomic distance.

588

589 **Enrichment of expressed genes**

590 To evaluate the activity of gene expression, we downloaded the RNA-seq data from ENCODE
591 (See Data), merged the biological replicates of RNA-seq data, and computed the average
592 FPKM for each gene. Genes with FPKM > 5 were deemed as expressed genes. For each TAD
593 level, we compute the density of expressed gene as the number of expressed genes per 10Kb.
594 For TADs with nested structures, genes covered by the inner level TADs are excluded in the
595 calculation of gene density for outer TADs.

596

597 **Enrichment of CTCF or cohesin protein signals**

598 To compute the enrichment of CTCF (or cohesin protein) signals at the identified boundaries
599 and their surrounding regions, we computed the average CTCF (or cohesin proteins) signals
600 from ChIP-seq data at the identified boundaries and the bins within their 10bins flanking regions.
601 The processed signals in bigwig file was used in this process.

602

603 **Epigenetic state enrichment**

604 We downloaded the IDEAS segmentation (see Data), which segments the genome into 36
605 epigenetic states based on 10 epigenomic marks [23]. We used it to evaluate the enrichment of
606 epigenetic state in the identified (sub)TADs and boundaries. Let n_i denote the total number of
607 200bp windows that have IDEAS-assigned epigenetic states at a TAD boundary i , and $n_{s,i}$
608 denote the number of 200bp windows annotated as state s at a TAD boundary i . For a given
609 state s , its enrichment in a set of M boundaries is computed as

$$E(s) = \frac{\sum_{i=1}^M n_{s,i} + 1}{B_s \sum_{i=1}^M n_i + 1}$$

610 where B_s is the proportion of state s in the whole genome. The 1's in the formula of $E(s)$ are
611 added to avoid dividing by 0.

612

613 **A/B compartments calling**

614 We used CscoreTool [39] to infer A/B compartments from mouse G1E-ER4 Hi-C data (10Kb
615 resolution, default parameter). The A/B compartments is determined by correlation coefficient
616 between compartment score and ATAC-seq signal. If a positive correlation coefficient is
617 observed, then regions with score>0 are in compartment A. Otherwise, if the correlation
618 coefficient is below 0, the regions with score < 0 are in compartment A. We reversed the
619 compartment scores on the chromosomes that has correlation coefficient < 0. Thus,
620 compartment A is shown with positive score and compartment B is shown with negative score.

621

622 **Data**

623 **Hi-C data:** The human Hi-C data is obtained from Rao et al. 2014 (GEO accession number:
624 GSE63525). Among them, three cell types (B-lymphoblastoid cells (GM12878), umbilical vein
625 endothelial cells (HUVEC) and erythrocytic leukemia cells (K562)) were included in this study.
626 The normalized (by Knight-Ruiz balancing method) Hi-C matrices at 5Kb, 10Kb and 25Kb
627 resolutions were used in this study. The mouse Hi-C data is obtained from Hsu et al. 2017

628 [32](GEO accession number: GSE95476). The 10Kb raw Hi-C matrices from G1E-ER4 and two
629 Brd2 knockouts were used in this study.

630

631 **Transcriptomic data:** The gene expression data were downloaded from the ENCODE project
632 (<https://www.encodeproject.org/>). The processed signal (FPKM) was used to measure the
633 expression activity.

634

635 **Epigenomic data:** The histone modification data were downloaded from the NIH Roadmap
636 Epigenomics project (<http://www.roadmapepigenomics.org/>), including H2A.Z, H3K27ac,
637 H3K27me3, H3K36me3, H3K4me1, H3K4me2, H3K4me3, H3K79me2, H3K9ac, H3K9me3 and
638 H4K20me1. The ChIP-seq data of CTCF and cohesin protein (Rad21 and Smc3) were
639 downloaded from ENCODE project (<https://www.encodeproject.org/>). The downloaded data
640 were in BigWig format. The 'bigWigAverageOverBed' was used to segment signal into windows
641 according to the resolution of Hi-C data. The mouse ChIP-seq data were downloaded from the
642 VISION project (<http://www.bx.psu.edu/~giardine/vision/>).

643

644 **Epigenetic states:** The IDEAS segmentation of the 6 ENCODE cell type/tissues (GM12878,
645 H1h-ESC, Hela-S3, HepG2, HUVEC, K562) was downloaded from ([http://main.genome-
647 browser.bx.psu.edu/](http://main.genome-
646 browser.bx.psu.edu/)). The 36-state IDEAS model trained on 10 marks (H3K4me1, H3K4me2,
648 H3K4me3, H3K9ac, H3K27ac, H3K27me3, H3K36me3, H3K20me1, PolII and CTCF), as well
as DNase-seq and Faire-seq, was applied to this study.

649

650

651 **Figure Legends**

652 **Figure 1 | Overview of the OnTAD pipeline.** **a**, OnTAD uses a sliding diamond-shaped
653 window to calculate the average contact frequency within the window at each locus on the
654 genome. The five loci marked by letters 'a'-'e' are examples being evaluated as potential TAD
655 boundaries, with 'd' being a clear false positive. **b**, Identification of candidate TAD boundaries in
656 OnTAD. Blue curve: the average contact frequency of the diamond-shaped windows, calculated
657 at different window sizes (W) and different loci. Red arrows: the location of significant local
658 minimums of the average contact frequency, i.e. candidate TAD boundaries. **c**, OnTAD
659 assembles candidate boundary pairs using a Dynamic Programming algorithm (see methods) **d**,
660 Visualization of the final output from OnTAD. In the genome browser, the identified hierarchical
661 TAD is displayed as a series of horizontal bars, where each (sub)TAD is represented as a
662 horizontal bar colored according to its TAD level.

663

664 **Figure 2 | Evaluation of TAD calling methods.** **a**, Average ChIP-Seq signal at TAD
665 boundaries and surrounding regions (+/- 10 bins) (from left to right, CTCF, SMC3 and RAD21).
666 **b**, Proportions of Hi-C signal variability explained by the called TADs (measured by TAD-adjR²)
667 at different genomic distance between two interacting loci. (Average TAD-adjR²: OnTAD: 0.33,
668 Arrowhead: 0.26, DomainCaller: 0.26, rGMAP: 0.23 and TADtree: 0.06). **c-e**, Reproducibility of
669 TAD boundaries (Jaccard index): **c**, between two biological replicates (GM12878, 10Kb) **d**,
670 between resolutions (5Kb vs 10Kb) and (10Kb vs 25Kb). **e**, across different down sampled
671 sequencing depths (GM12878, original vs 1/4, 1/8, 1/16 and 1/32 of the original sequencing
672 depth, raw data was used). Note: TADtree was not included in **d**, because it has difficulty
673 handling data with 5Kb resolution due to its large memory consumption. It also has difficulty for
674 chr1-3 at 10Kb resolution either. Thus these three chromosomes were excluded for all TAD
675 callers in all comparisons.

676

677 **Figure 3 | Hierarchical TADs are more active than singletons.** **a**, An illustration of
678 hierarchical levels of TADs. The levels are assigned from external to internal. The TADs
679 covered by cyan dash line are assigned to level 1, by blue dash line are assigned to level 2, by
680 orange dash line are assigned to level 3, and singletons are also assigned to level 1 (cyan). **b**,
681 mean CTCF signal at the boundaries specific to hierarchical TADs (light green), specific to
682 singletons (cyan), and shared between hierarchical TADs and singletons (orange). The
683 boundaries of hierarchical TADs have the highest enrichment of CTCF signal. **c-d**, Enrichment
684 of epigenetic states at the regions covered by different levels of TADs. The enrichment (fold

685 change) of active states (marked in orange in **c**) increases as the TAD level increases. The
686 trend is visualized for the states of Tss, Enh and PromCtcf in **d**. The whole-genome average is
687 used as the background for calculating enrichments. **e-f**, Density of expressed gene in different
688 levels of TADs in GM12878 (**e**) and K562 (**f**).
689

690 **Figure 4 | Hub-boundaries are highly active in gene regulation.** **a**, An illustration of the TAD
691 boundary levels. The boundary levels are defined as the maximum number of TADs that use a
692 boundary on either its left or right side. The yellow, purple and red dots refer to boundaries of
693 level 1, 2, and 3, respectively. **b**, Enrichment of epigenetic states at different levels of TAD
694 boundaries. Hub-boundaries (i.e. boundaries with level =5) are significantly enriched with Tss
695 related states than others. (Active epigenetic states are marked in orange) **c**, Distribution of
696 gene expression levels for genes whose transcription start sites overlap with TAD boundaries.
697 Genes are classified by the level of TAD boundaries. **d**, Illustration of hierarchical TAD and
698 asymmetric loop extrusion. The red boundary denotes the ‘anchor’ site that starts the loop
699 extrusion in asymmetric loop extrusion model. Boundaries in other colors are the stopping sites
700 of the loop extrusion. The hierarchical TADs are formed by multiple stops of the loop extrusion
701 that share the same start site. **e**, TFs enriched (Fold Change >2) at hub-boundaries in
702 GM12878 and K562 cell lines. The fold change of ChIP-seq TF peaks at hub-boundaries (level
703 =5) against level 1 boundaries is shown.
704

705 **Figure 5 | subTADs exhibit distinctive epigenetic profiles.** The captured region is
706 chr19:11.3Mb – 12.2Mb in mouse G1E-ER4. The Hi-C heatmap shows a nested TAD structure
707 in this region. OnTAD results are displayed in the genome browser track: blue line denotes level
708 1 TAD, green line denotes level 2 TAD, purple denotes level 3 TAD and orange denotes level 4
709 TAD. The two subTADs (orange lines) exhibit distinctive epigenetic features, with one enriched
710 with repressive signals (H3K27me3) and silenced expression (low RNA-Seq signal) and the
711 other enriched with active signals (H3K27ac, H3K4me3, and H3K36me3) and expression (high
712 RNA-Seq signal). The shared boundary (marked by dash box) between these two subTADs has
713 no CTCF peak, indicating the formation of these two subTADs may not involve loop extrusion.
714

715 **Supplementary figure 1 | Illustration of convoluted TAD structures.** **a**, Candidate TADs (a,c)
716 and (b,d) are both suboptimal, as their scores may be driven by a real TAD (b,c). **b**, Two real
717 TADs (a,c) and (b,c) are nested, which makes the score of (a,c) convoluted with the score of

718 (b,c). **c**, Real TADs (a,c) and (b,d) are partially overlapping, which may be recaptured as nested
719 TADs (b,c), (a,c) and (a,d).

720

721 **Supplementary figure 2 | Illustration of the recursive TAD calling algorithm.** **a**, At the first
722 step of the algorithm, the entire Hi-C matrix is partitioned into two matrices, the one forming the
723 largest right-most TAD (i.e. triangles marked in black) and the remaining part, according to a
724 score function. Then the same function is called on each sub-matrix to recursively identify
725 nested TAD structures. **b**, Each recursion step identifies the best set of TADs in its matrix under
726 consideration according to the score function, and returns the TAD calls back to its parent until
727 the root.

728

729 **Supplementary figure 3 | TAD reproducibility under different measurements.** **a**, Adjusted
730 rand index between TADs from two biological replicates (GM12878, 10Kb). **b**, Adjusted rand
731 index across TADs from Hi-C data in multiple resolutions (GM12878, 5Kb, 10Kb and 25Kb).
732 TADtree is not included because it has difficulty finishing the computation on high resolution
733 data due to its high memory consumption. **c**, Adjusted rand index between TADs from Hi-C data
734 in original sequencing depth and in different down sampled sequencing depth (GM12878, 1/4,
735 1/8, 1/16 and 1/32 of original sequencing depth).

736

737 **Supplementary figure 4 | Enrichment of epigenetic states at the boundaries of different**
738 **levels of TADs.** Enrichment of epigenetic states at the regions covered by different levels of
739 TADs. The enrichment (fold change) of active states (orange states) increases as the TAD level
740 increases. **a**, K562 **b**, Huvec

741

742 **Supplementary figure 5 | Comparison between boundaries and inside TADs** **a**, Distribution
743 of RNA-seq signal (FPKM) at the boundaries (blue) and within TADs (red) **b**, Enrichment of
744 active epigenetic states at the TAD boundaries (solid line) versus inside TADs (dashed line). Y-
745 axis denotes fold enrichment of three active epigenetic states (Tss, Enh and PromCtcf). X-axis
746 denotes the boundaries and TADs at different levels.

747

748 **Supplementary figure 6 | Distribution of the levels of TAD boundaries.**

749

750 **Supplementary figure 7 | Protein-protein interaction network of hub-boundary-enriched**
751 **TFs from STRING database.** Each node denotes a TF that are at least 2-fold enriched at hub-

752 boundary over level1 boundary (n=37). Each edge denotes the interaction potential between
753 two TFs, with thicker edges corresponding to higher interaction confidence. Interaction data was
754 downloaded from STRING database (<https://string-db.org/>)

755

756 **Supplementary figure 8 | Contact frequency is unbalanced between the two sides of**
757 **hierarchical TAD corners.** The regions around TAD corners are segregated into four
758 quadrants (1-4 on the top right figure). We then averaged contact frequency of each TAD corner
759 by quadrants. As shown in the heatmap, the majority quadrant 2 and 3 shows unequal average
760 contact frequencies, suggesting that the inner TADs tend to be formed on one side of the outer
761 TADs, rather than on both sides. Quadrant 1 has the highest average contact frequency
762 because it is within TADs.

763

764 **Supplementary Figure 9 | Comparison of OnTAD results between raw Hi-C and**
765 **normalized Hi-C in GM12878 (10kb).** **a**, Enrichment of CTCF signal at identified TAD
766 boundaries and surrounding regions (+/- 10 bins) in raw Hi-C matrix and normalized Hi-C matrix.
767 Y-axis: The average ChIP-Seq signal. **b**, TAD-adjR² of OnTAD results at difference genomic
768 distance in raw Hi-C matrix and normalized Hi-C matrix. The results on normalized data show a
769 slightly higher enrichment of CTCF at boundary and a higher TAD-adjR². The normalized Hi-C
770 matrices were generated by Knight-Ruiz balancing [40] method. **c**, The proportion of boundaries
771 identified in raw data that are recovered in normalized data. Grey: exact match; Green: one bin
772 offset allowed when matching the boundaries identified in raw and normalized data. Half of the
773 boundaries identified in the raw data precisely match with the boundaries identified in the
774 normalized data. If we allow one bin offset when matching the locations of the boundaries, over
775 71% of the high-level TAD boundaries (level 2+) are matched between the results from raw data
776 and normalized data.

777

778 **Supplementary Figure 10| Similarity between the (sub)TADs identified at Lsize = 5 and at**
779 **other Lsizes.**

780

781 **Supplementary Table 1 | Comparison of running time of different methods on high**
782 **resolution Hi-C data (GM12878 10Kb) (unit: seconds).**

783

784 **Supplementary Table 2 | Number of TADs on each side of a boundary that share this**
785 **boundary (GM12878 10Kb).**

786

787 **Supplementary Table 3 | The FDR and number of TADs under each penalty value.**
788 **(GM12878, average on 100 permutations)**

789

790 **Supplementary Table 4 | The FDR and number of TADs under each penalty value. (G1E-**
791 **ER4, average on 100 permutations)**

792

793 **Supplementary Table 5 | The FDR and number of TADs under each Lsize. (GM12878,**
794 **average on 100 permutations)**

795

796 **Supplementary File1 | Commands for operating other TAD calling methods.**

797

798 **Declarations**

799 **Acknowledgments**

800 This work was supported by the NIH R01 GM121613, NIH R01GM109453 and NIH R24
801 DK106766, NIH training grant T32 GM102057 (CBIOS training program to The Pennsylvania
802 State University), a Huck Graduate Research Innovation Grant, and 4D Nucleome NIH Initiative
803 DK107980 (Center for 3D Structure and Physics of the Genome).

804

805 **Availability of data and materials**

806 OnTAD is available at <https://github.com/anlin00007/OnTAD>.

807

808 **Authors' contributions**

809 YZ and LA implemented OnTAD. YZ and QL conceived the method. LA, TY, GX and JY
810 conducted the analysis. LA, YZ, QL, TY and RCH wrote the manuscript with assistance from the
811 other authors. JN assisted the interpretation of the results. All authors read and approved the
812 final manuscript.

813

814 **Competing interests**

815 The authors declare that they have no competing interests.

816

817 **Reference**

818 1. Won H, De La Torre-Ubieta L, Stein JL, Parikhshak NN, Huang J, Opland CK, et al. Chromosome
819 conformation elucidates regulatory relationships in developing human brain. *Nature*. 2016;

820 2. Dekker J, Rippe K, Dekker M, Kleckner N. Capturing chromosome conformation. *Science* (80-).
821 2002;
822 3. Dekker J, Marti-Renom MA, Mirny LA. Exploring the three-dimensional organization of
823 genomes: Interpreting chromatin interaction data. *Nat. Rev. Genet.* 2013.
824 4. Fullwood MJ, Ruan Y. ChIP-based methods for the identification of long-range chromatin
825 interactions. *J Cell Biochem.* 2009;
826 5. Mumbach MR, Rubin AJ, Flynn RA, Dai C, Khavari PA, Greenleaf WJ, et al. HiChIP: Efficient
827 and sensitive analysis of protein-directed genome architecture. *Nat Methods.* 2016;
828 6. Dekker J. The three “C” s of chromosome conformation capture: Controls, controls, controls.
829 *Nat Methods.* 2006;
830 7. Dostie J, Richmond TA, Arnaout RA, Selzer RR, Lee WL, Honan TA, et al. Chromosome
831 Conformation Capture Carbon Copy (5C): A massively parallel solution for mapping interactions
832 between genomic elements. *Genome Res.* 2006;
833 8. Zhao Z, Tavoosidana G, Sjölander M, Göndör A, Mariano P, Wang S, et al. Circular
834 chromosome conformation capture (4C) uncovers extensive networks of epigenetically
835 regulated intra- and interchromosomal interactions. *Nat Genet.* 2006;
836 9. Lieberman-Aiden E, Van Berkum NL, Williams L, Imakaev M, Ragoczy T, Telling A, et al.
837 Comprehensive mapping of long-range interactions reveals folding principles of the human
838 genome. *Science* (80-). 2009;
839 10. Dixon JR, Gorkin DU, Ren B. Chromatin Domains: The Unit of Chromosome Organization.
840 *Mol. Cell.* 2016.
841 11. Dixon JR, Selvaraj S, Yue F, Kim A, Li Y, Shen Y, et al. Topological domains in mammalian
842 genomes identified by analysis of chromatin interactions. *Nature.* 2012;
843 12. Dixon JR, Jung I, Selvaraj S, Shen Y, Antosiewicz-Bourget JE, Lee AY, et al. Chromatin
844 architecture reorganization during stem cell differentiation. *Nature.* 2015;
845 13. Shin H, Shi Y, Dai C, Tjong H, Gong K, Alber F, et al. TopDom: An efficient and deterministic
846 method for identifying topological domains in genomes. *Nucleic Acids Res.* 2015;
847 14. Crane E, Bian Q, McCord RP, Lajoie BR, Wheeler BS, Ralston EJ, et al. Condensin-driven
848 remodelling of X chromosome topology during dosage compensation. *Nature.* 2015;
849 15. Weinreb C, Raphael BJ. Identification of hierarchical chromatin domains. *Bioinformatics.*
850 2016;
851 16. Yu W, He B, Tan K. Identifying topologically associating domains and subdomains by
852 Gaussian Mixture model and Proportion test. *Nat Commun.* 2017;
853 17. Rao SSP, Huntley MH, Durand NC, Stamenova EK, Bochkov ID, Robinson JT, et al. A 3D map
854 of the human genome at kilobase resolution reveals principles of chromatin looping. *Cell.* 2014;
855 18. Norton HK, Emerson DJ, Huang H, Kim J, Titus KR, Gu S, et al. Detecting hierarchical genome
856 folding with network modularity. *Nat Methods.* 2018;
857 19. Haddad N, Vaillant C, Jost D. IC-Finder: Inferring robustly the hierarchical organization of
858 chromatin folding. *Nucleic Acids Res.* 2017;
859 20. Fraser J, Ferrai C, Chiariello AM, Schueler M, Rito T, Laudanno G, et al. Hierarchical folding
860 and reorganization of chromosomes are linked to transcriptional changes in cellular
861 differentiation. *Mol Syst Biol.* 2015;
862 21. Sanborn AL, Rao SSP, Huang S-C, Durand NC, Huntley MH, Jewett Al, et al. Chromatin
863 extrusion explains key features of loop and domain formation in wild-type and engineered

864 genomes. *Proc Natl Acad Sci.* 2015;

865 22. Ho JWK, Jung YL, Liu T, Alver BH, Lee S, Ikegami K, et al. Comparative analysis of metazoan

866 chromatin organization. *Nature.* 2014;

867 23. Zhang Y, An L, Yue F, Hardison RC. Jointly characterizing epigenetic dynamics across multiple

868 human cell types. *Nucleic Acids Res.* 2016;

869 24. Dunham I, Kundaje A, Aldred SF, Collins PJ, Davis CA, Doyle F, et al. An integrated

870 encyclopedia of DNA elements in the human genome. *Nature.* 2012;

871 25. Schmitt AD, Hu M, Jung I, Xu Z, Qiu Y, Tan CL, et al. A Compendium of Chromatin Contact

872 Maps Reveals Spatially Active Regions in the Human Genome. *Cell Rep.* 2016;

873 26. Ganji M, Shaltiel IA, Bisht S, Kim E, Kalichava A, Haering CH, et al. Real-time imaging of DNA

874 loop extrusion by condensin. *Science* (80-). 2018;

875 27. Zheng M, Tian SZ, Capurso D, Kim M, Maurya R, Lee B, et al. Multiplex chromatin

876 interactions with single-molecule precision. *Nature.* 2019;566:558–62.

877 28. Kschonsak M, Merkel F, Bisht S, Metz J, Rybin V, Hassler M, et al. Structural Basis for a

878 Safety-Belt Mechanism That Anchors Condensin to Chromosomes. *Cell.* 2017;

879 29. Gerstein MB, Kundaje A, Hariharan M, Landt SG, Yan KK, Cheng C, et al. Architecture of the

880 human regulatory network derived from ENCODE data. *Nature.* 2012;

881 30. Wang J, Zhuang J, Iyer S, Lin XY, Whitfield TW, Greven MC, et al. Sequence features and

882 chromatin structure around the genomic regions bound by 119 human transcription factors.

883 *Genome Res.* 2012;

884 31. Wang J, Zhuang J, Iyer S, Lin XY, Greven MC, Kim BH, et al. Factorbook.org: A Wiki-based

885 database for transcription factor-binding data generated by the ENCODE consortium. *Nucleic*

886 *Acids Res.* 2013;

887 32. Hsu SC, Gilgenast TG, Bartman CR, Edwards CR, Stonestrom AJ, Huang P, et al. The BET

888 Protein BRD2 Cooperates with CTCF to Enforce Transcriptional and Architectural Boundaries.

889 *Mol Cell.* 2017;

890 33. Rowley MJ, Nichols MH, Lyu X, Ando-Kuri M, Rivera ISM, Hermetz K, et al. Evolutionarily

891 Conserved Principles Predict 3D Chromatin Organization. *Mol Cell.* 2017;67:837–852.e7.

892 34. Rowley MJ, Corces VG. Organizational principles of 3D genome architecture. *Nat Rev Genet.*

893 2018;

894 35. Oudelaar AM, Davies JOJ, Hanssen LLP, Telenius JM, Schwessinger R, Liu Y, et al. Single-allele

895 chromatin interactions identify regulatory hubs in dynamic compartmentalized domains. *Nat*

896 *Genet.* 2018;

897 36. Bintu B, Mateo LJ, Su JH, Sinnott-Armstrong NA, Parker M, Kinrot S, et al. Super-resolution

898 chromatin tracing reveals domains and cooperative interactions in single cells. *Science* (80-).

899 2018;

900 37. Imakaev M, Fudenberg G, McCord RP, Naumova N, Goloborodko A, Lajoie BR, et al. Iterative

901 correction of Hi-C data reveals hallmarks of chromosome organization. *Nat Methods.* 2012;

902 38. Efron B. Size, power and false discovery rates. *Ann Stat.* 2007;

903 39. Zheng X, Zheng Y. CscoreTool: Fast Hi-C compartment analysis at high resolution.

904 *Bioinformatics.* 2018;

905 40. Knight PA, Ruiz D. A fast algorithm for matrix balancing. *IMA J Numer Anal.* 2013;

906

Figure 1

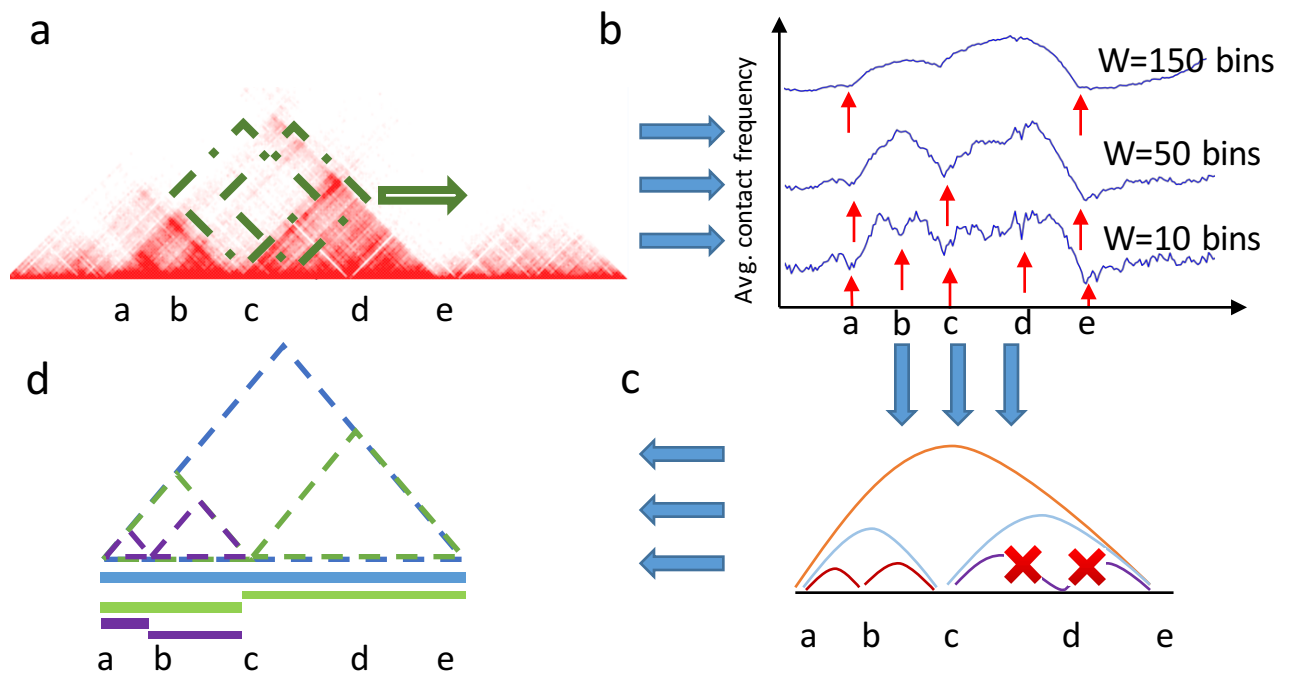
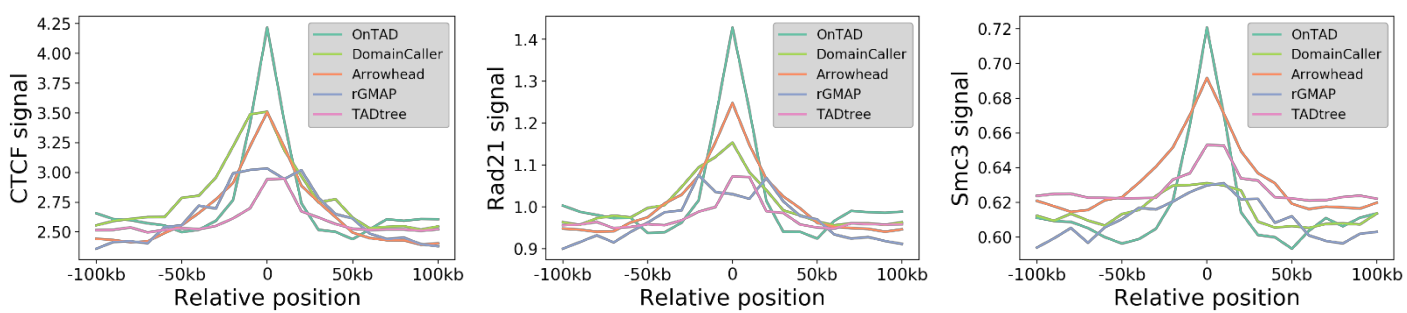
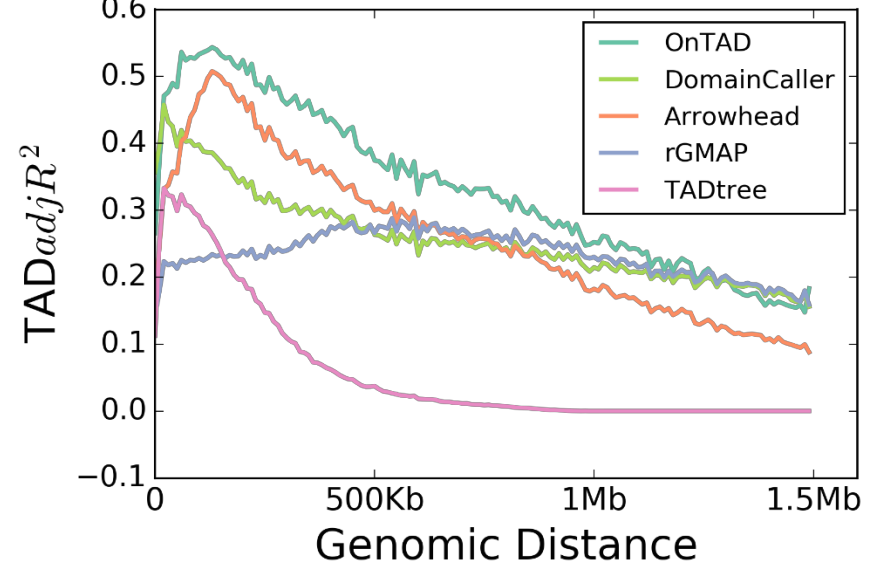


Figure 2

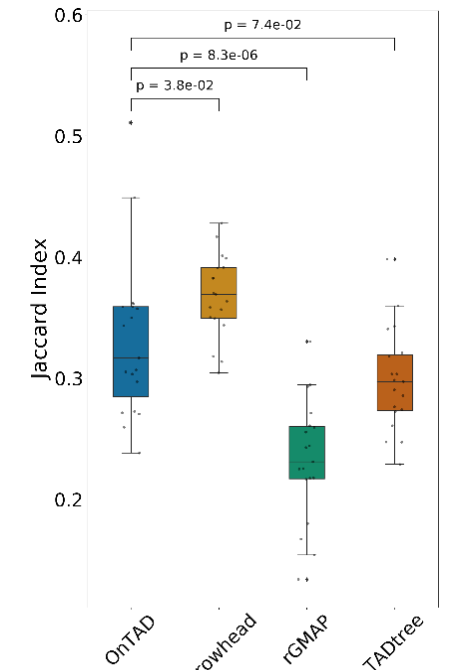
a



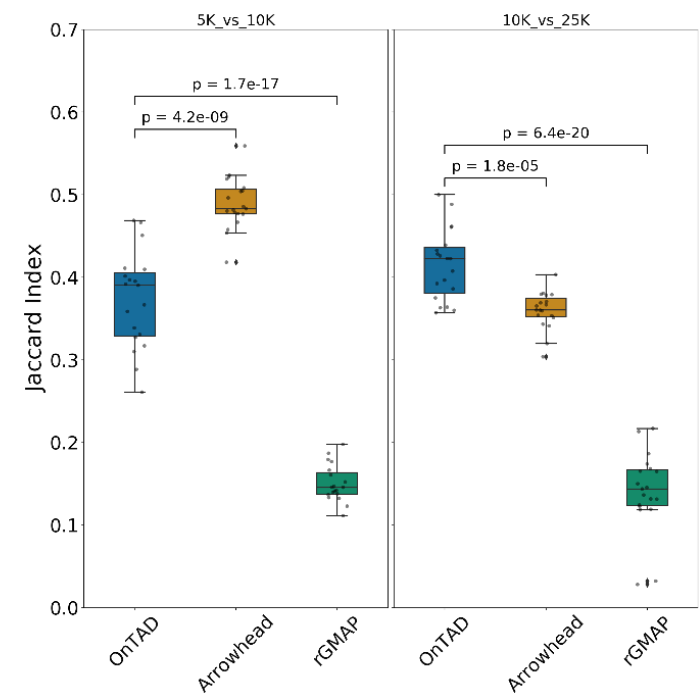
b



c



d



e

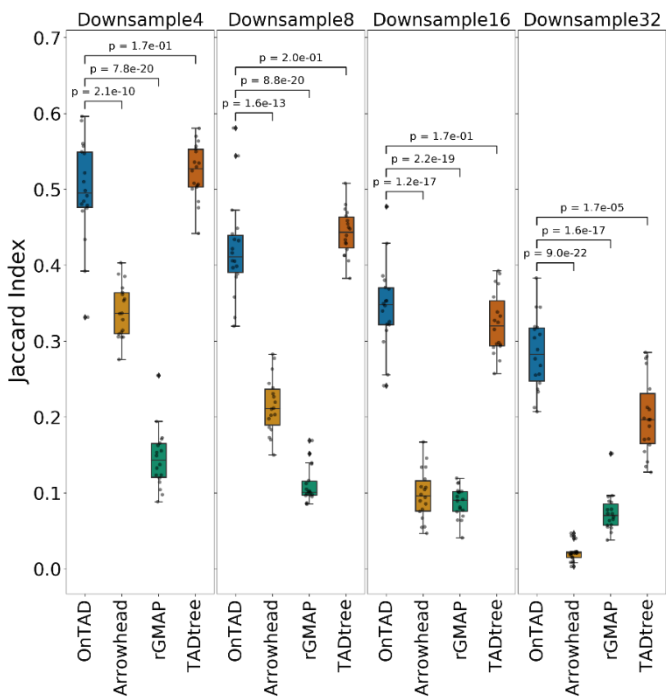


Figure 3

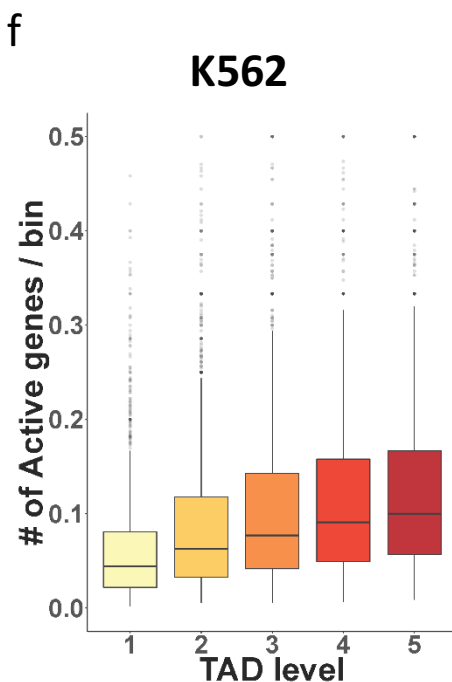
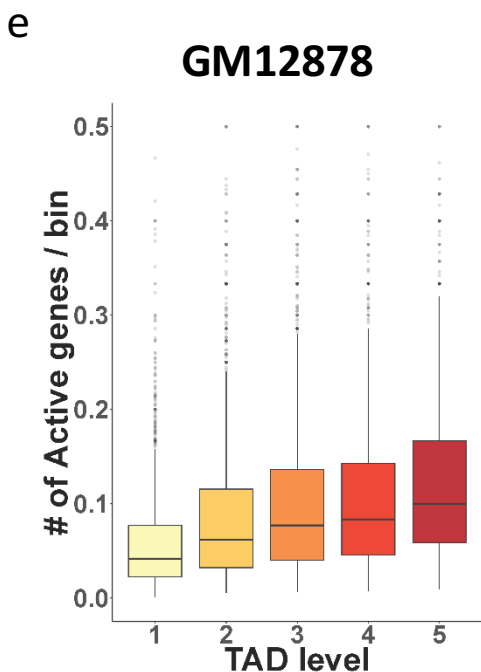
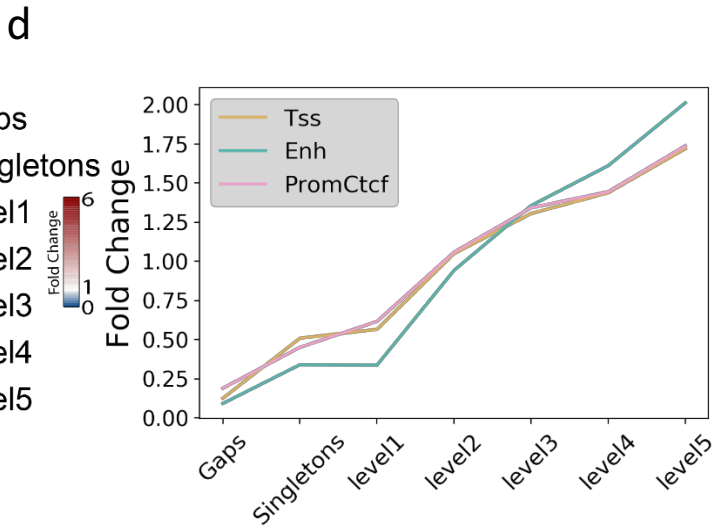
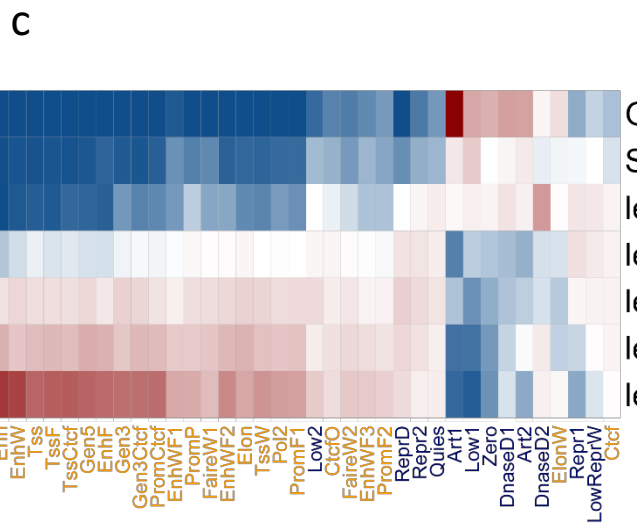
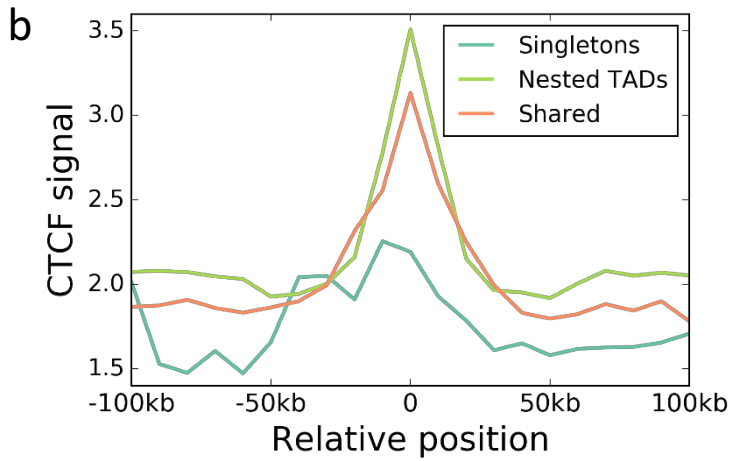
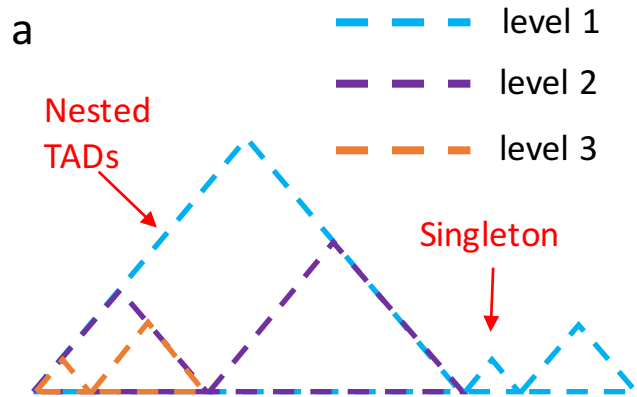


Figure 4

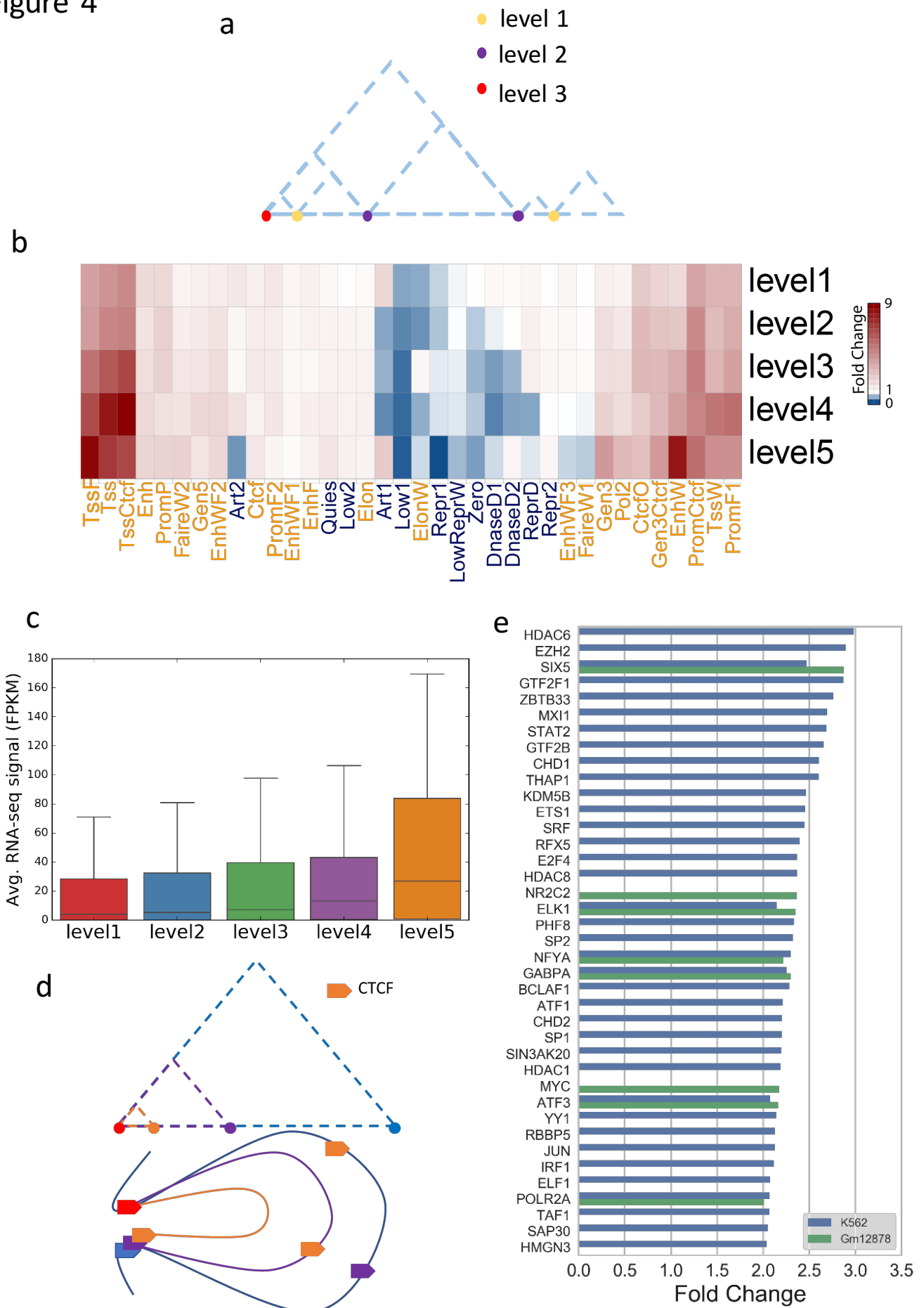
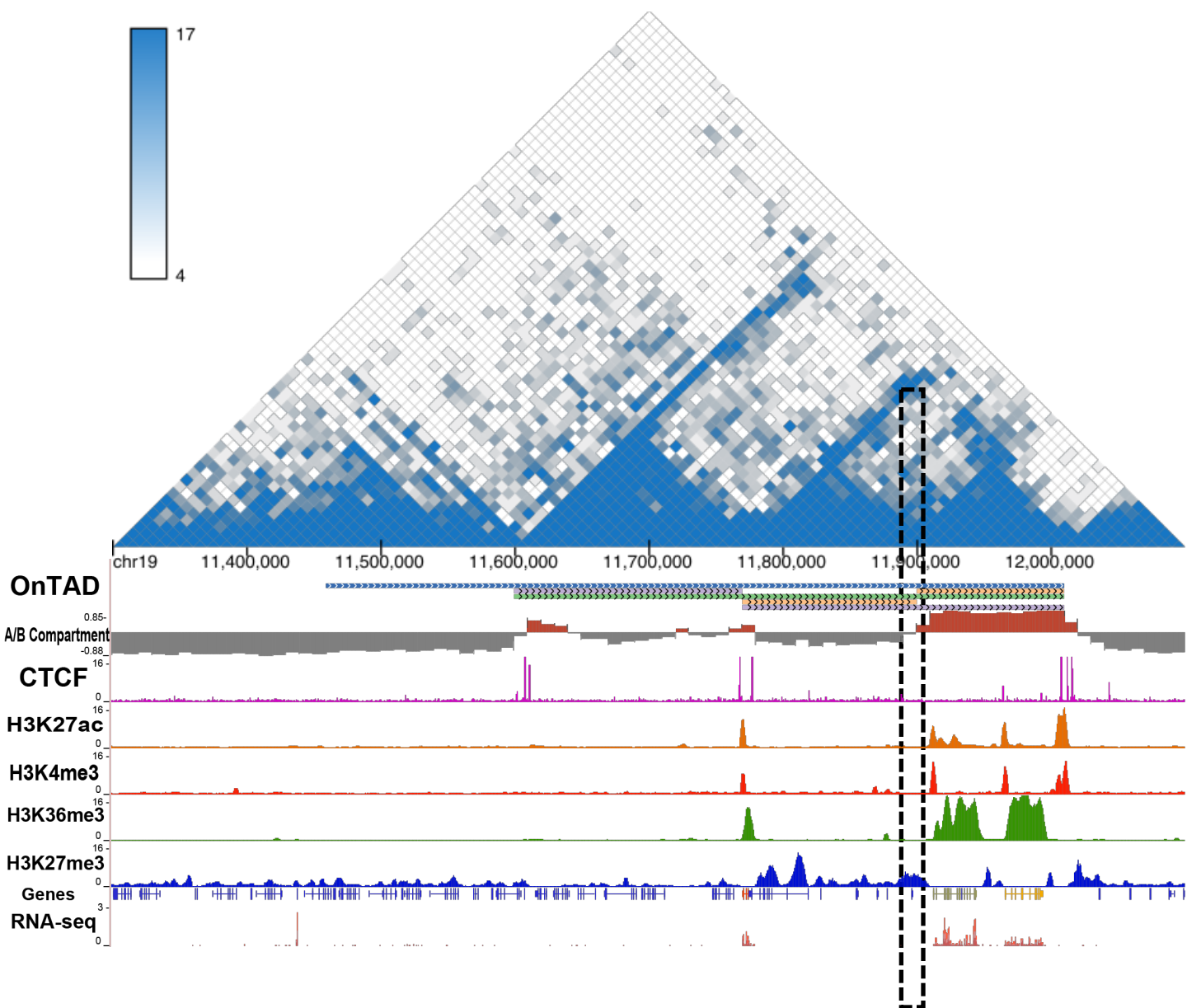
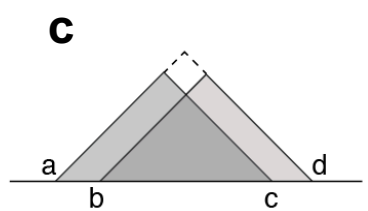
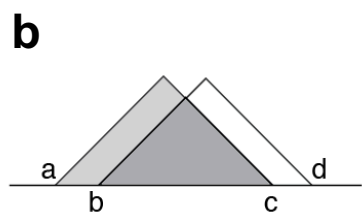
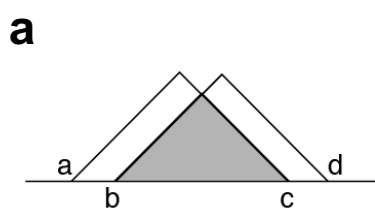


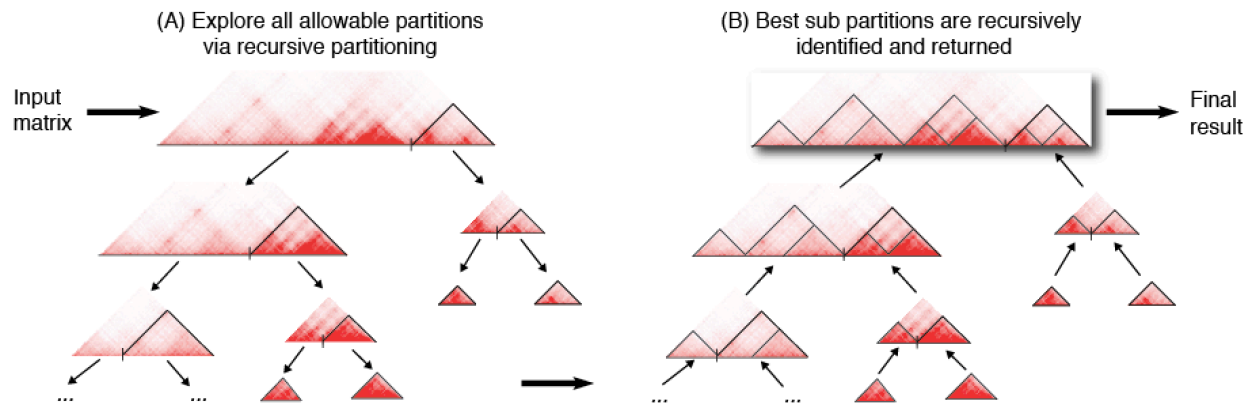
Figure 5



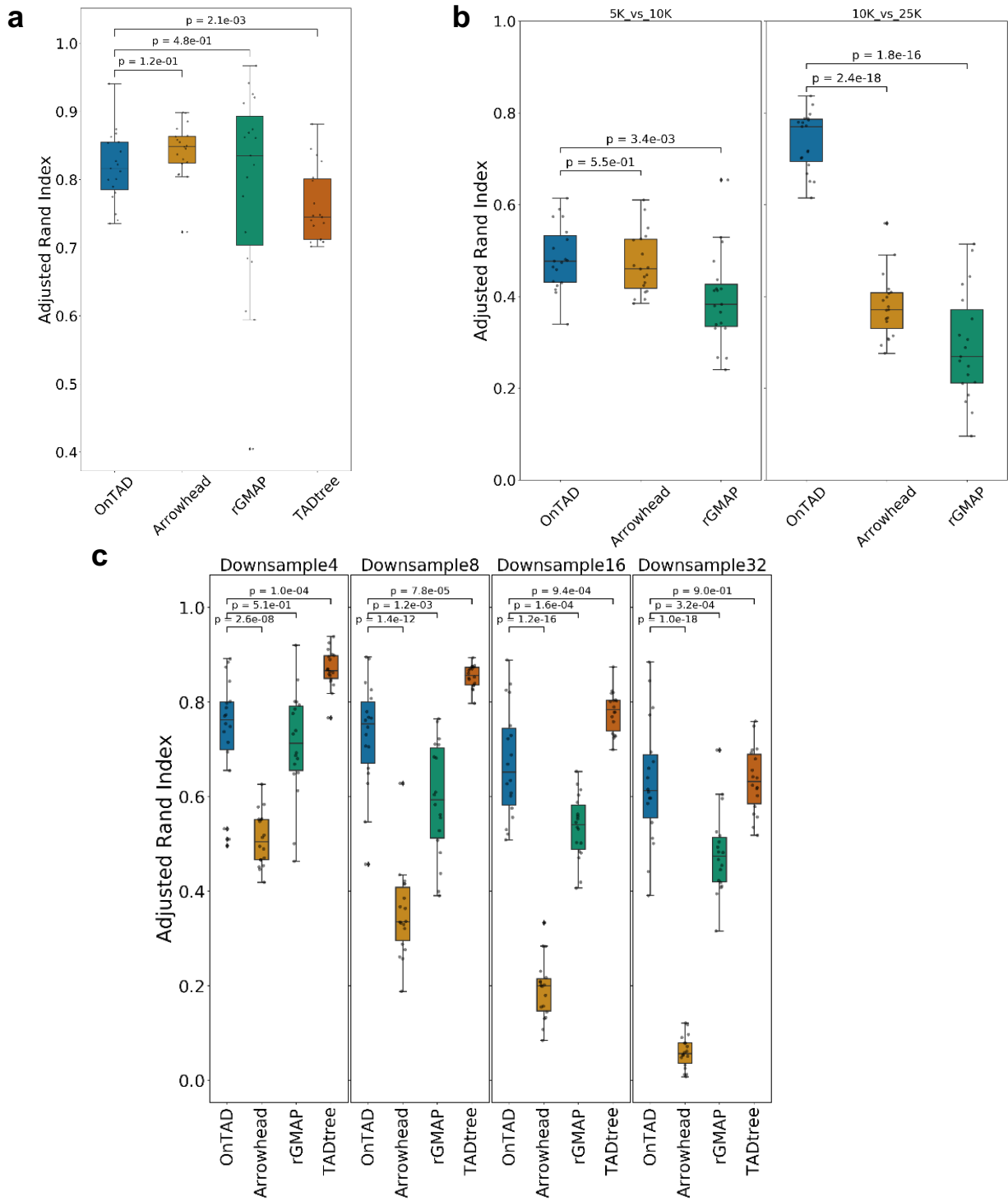
Supplementary figure 1



Supplementary figure 2

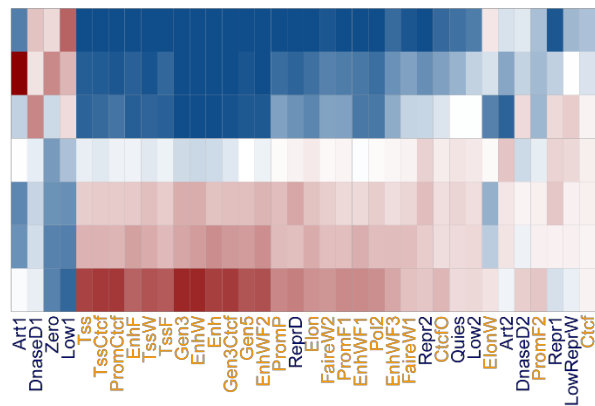


Supplementary figure 3

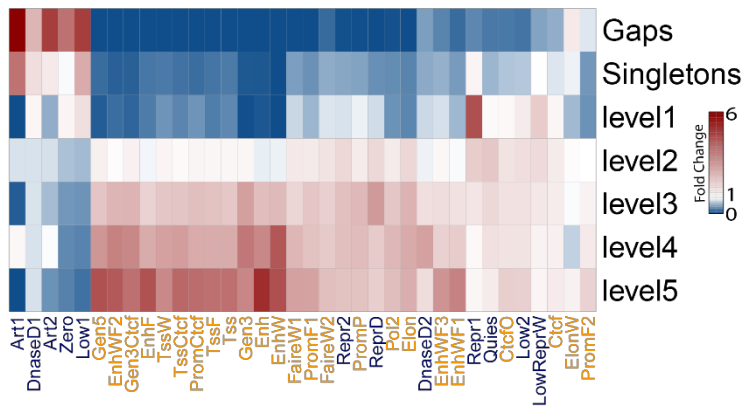


Supplementary figure 4

a

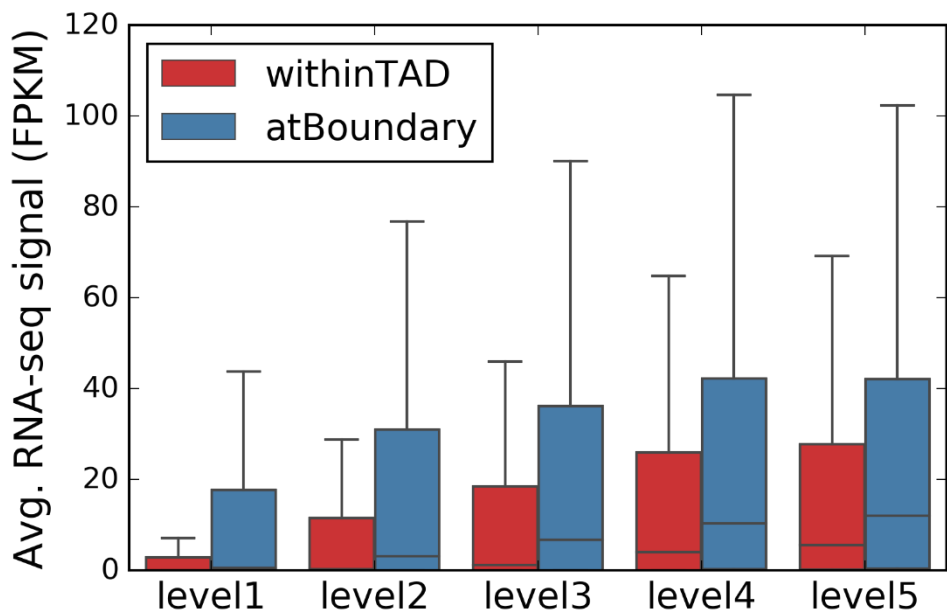


b

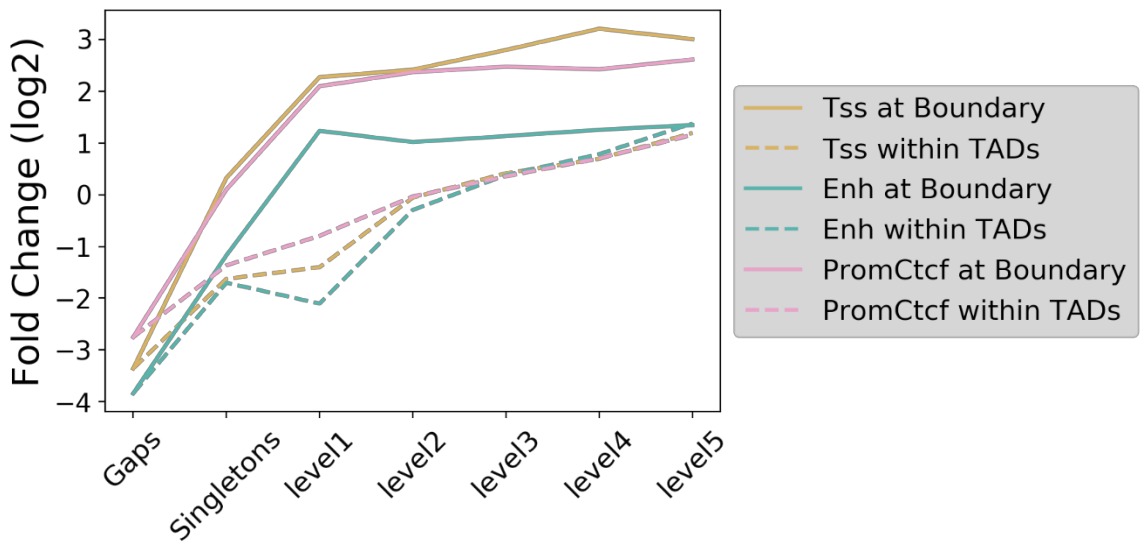


Supplementary figure 5

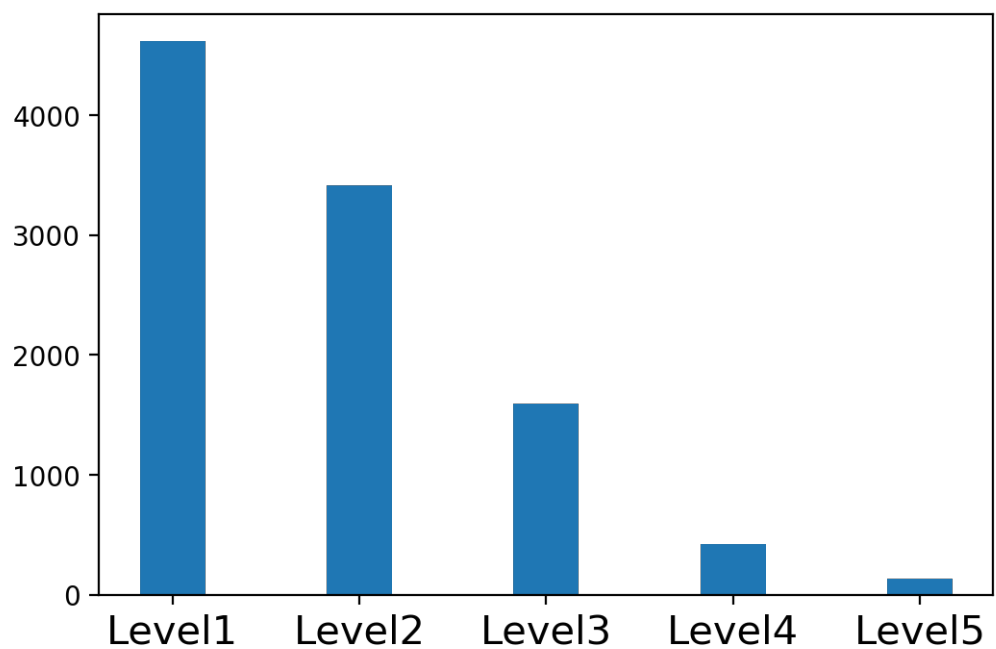
a



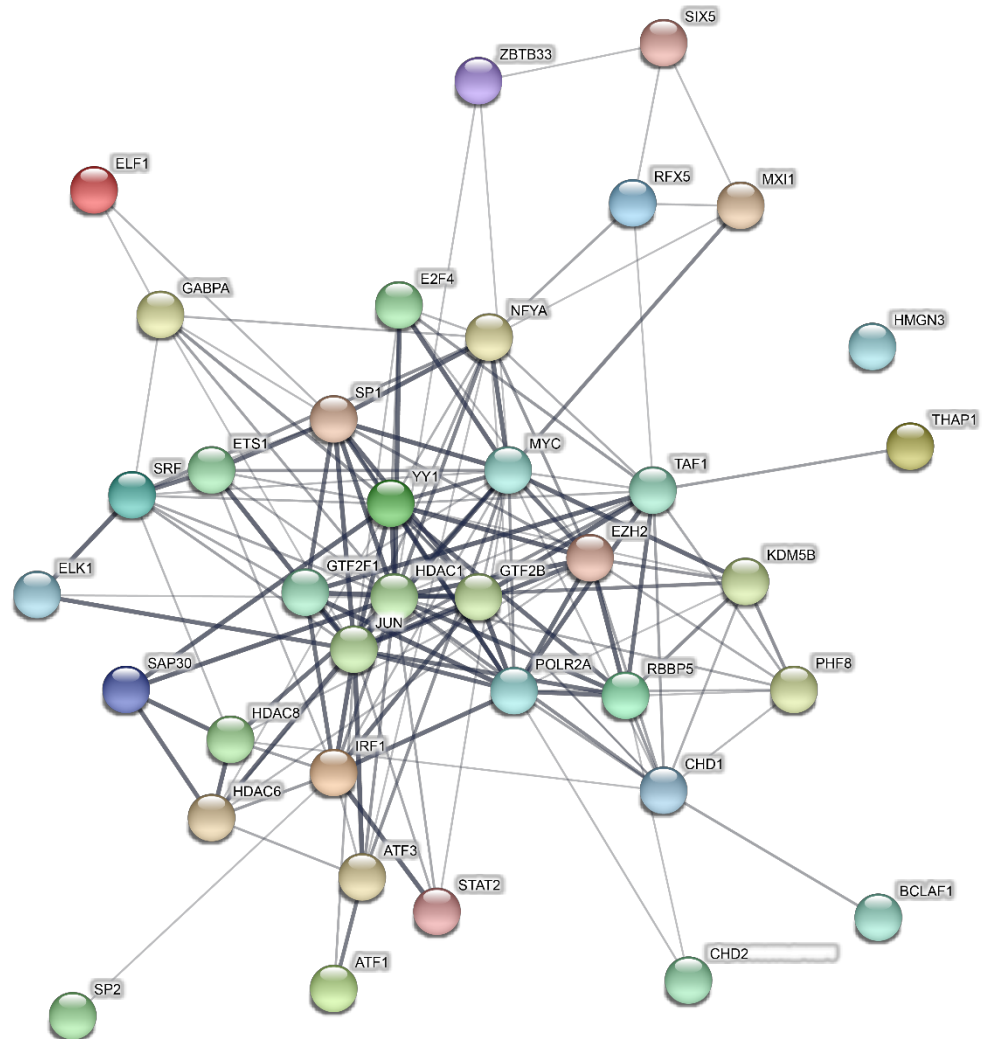
b



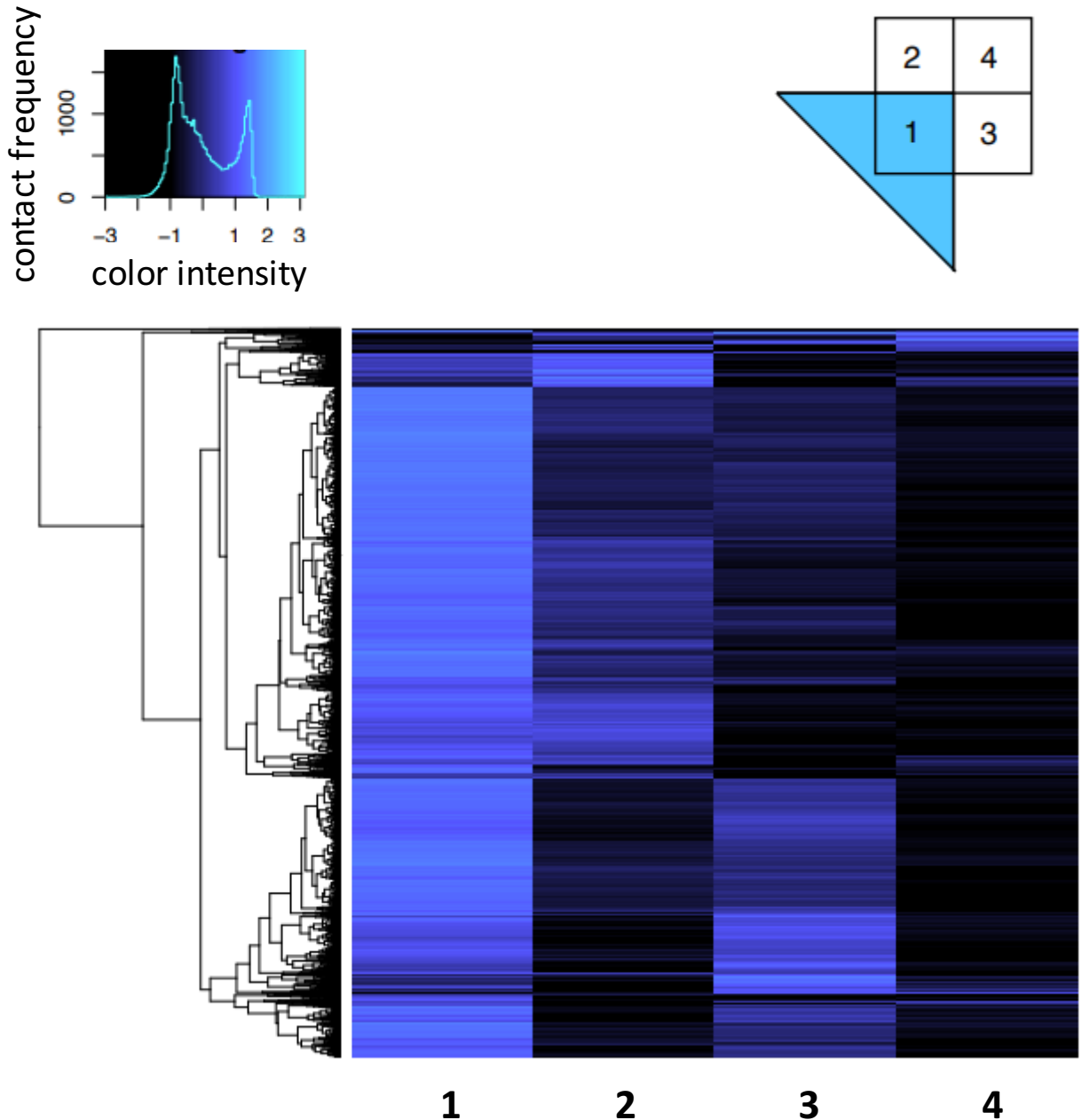
Supplementary figure 6



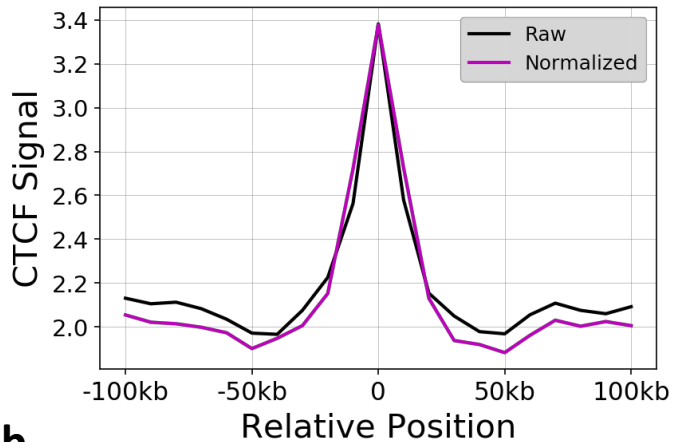
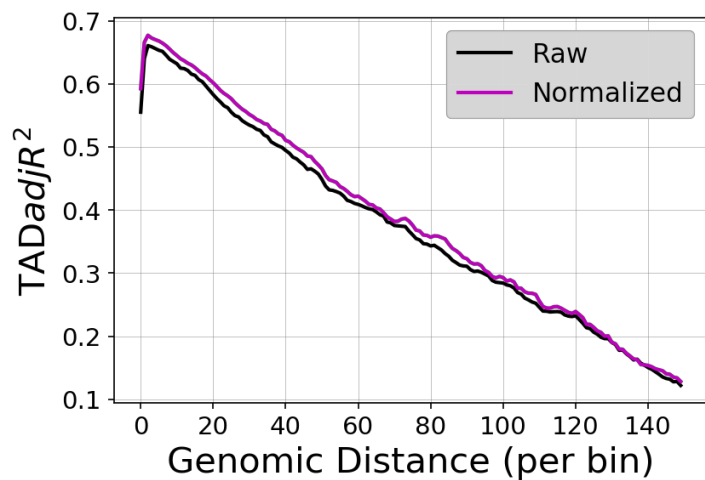
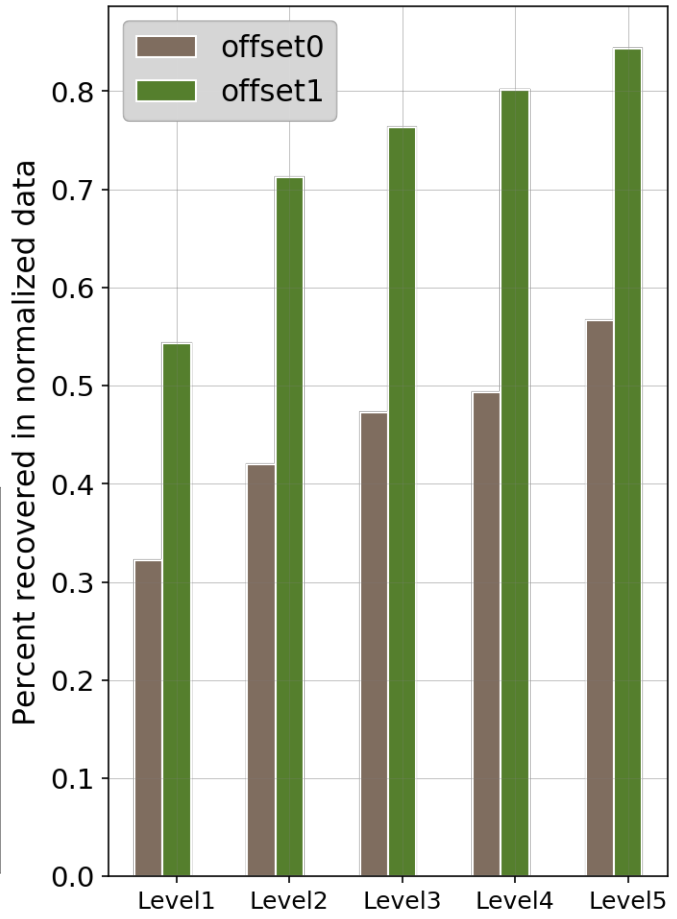
Supplementary figure 7



Supplementary figure 8



Supplementary figure 9

a**b****c**

Supplementary figure 10

